Optical conductivity of gapped math xmlns="http://www.w3.org/1998/Math/MathML">mrow>mi >α/mi>mtext>−/mtext>msub>mi mathvariant="script">T/mi>mn>3/mn>/msub>/mrow>/math> materials with a deformed flat band

Andrii Iurov, Liubov Zhemchuzhna, Godfrey Gumbs, and Danhong Huang

Phys. Rev. B **107**, 195137 — Published 19 May 2023

DOI: 10.1103/PhysRevB.107.195137

Optical conductivity of gapped α-$\mathcal{T}_3$ materials with a deformed flat band

Andrii Iurov[1*], Liubov Zhemchuzhna[1,2], Godfrey Gumbs[2,3], and Danhong Huang[4]
[1]*Department of Physics and Computer Science, Medgar Evers College of City University of New York, Brooklyn, NY 11225, USA*
[2]*Department of Physics and Astronomy, Hunter College of the City University of New York, 695 Park Avenue, New York, New York 10065, USA*
[3]*Donostia International Physics Center (DIPC), P de Manuel Lardizabal, 4, 20018 San Sebastian, Basque Country, Spain*
[4]*Space Vehicles Directorate, US Air Force Research Laboratory, Kirtland Air Force Base, New Mexico 87117, USA*

(Dated: May 8, 2023)

We derived and discussed the optical conductivity of α-$\mathcal{T}_3$ materials with a finite bandgap in their energy dispersions. In contrast with familiar α-$\mathcal{T}_3$ materials, this constitutes a non-trivial case since the flat band changes into a curved one and two other branch dispersion relations become nonlinear beyond the limiting cases for graphene and the dice-lattice. Such a unique band structure appears if the α-$\mathcal{T}_3$ material is irradiated by a circularly-polarized light non-resonantly. For this system, we have obtained optical conductivities at either zero or finite temperatures with nonzero or near-zero doping. Additionally, we have demonstrated that analytical expressions could be obtained for all types of gapped α-$\mathcal{T}_3$ materials, and meanwhile, provided closed-form analytical expressions for a gapped dice lattice. Our current studies reproduce known properties of optical conductivity in unirradiated α-$\mathcal{T}_3$ materials and silicene with two non-equivalent bandgaps, and furthermore, demonstrate some very interesting irradiation-enabled behaviors which are absent in any Dirac materials. The discovery of unusual properties for the optical conductivity of gapped α-$\mathcal{T}_3$ in this work is expected to have many promising device applications, such as photodetectors, optical modulators and metasurfaces.

I. INTRODUCTION

The recently proposed α-$\mathcal{T}_3$ model [1–3] describes electronic behaviors of a wide range of novel two-dimensional (2D) lattices with good precision. [4] The atomic build-up of an α-$\mathcal{T}_3$ material consists of a regular hexagon, similar to that of graphene (rim atom), with an additional atom at the center of the hexagon (a hub atom). [5] Consequently, such lattices are made up of three atoms per unit cell, which gives rise to additional rim-hub electronic hopping and a novel electron low-energy branch. [6] The calculation of electronic band structure of $\alpha - \mathcal{T}_3$ lattice has been based on a tight-binding model and analysis for the ratio of electron hopping coefficients between the atoms of hexagons (rim-rim hopping) and the hub atoms at the center of hexagons with one of the rim atoms. The ratio between hub-rim and rim-rim hopping coefficient is defined as a parameter α for $\alpha - \mathcal{T}_3$ lattice, which runs between 0 (graphene with completely decoupled atoms at centers of hexagons) and a dice lattice with $\alpha = 1$.

The most unusual characteristics of the α-$\mathcal{T}_3$ band energy structure is the presence of a flat band in their energy dispersions in addition to a regular Dirac cone, which remains stable under various external effects, such as electric and magnetic fields or impurities. [7] This unexpected, but yet relatively simple electronic energy dispersion, has stimulated a huge amount of research on the electronic, [8–13] magnetic, [14,15] optical, [16–19] transport, [20–22] tunneling [23–28] and collective-excitation [29,30] properties of α-$\mathcal{T}_3$ and even α-$\mathcal{T}_3$-based nanoribbons [31–34]. However, there is still one key issue remains to be addressed, i.e. how are these properties different from those of previously explored graphene. [35–38]

From a mathematical point of view, the α-$\mathcal{T}_3$ model is basically viewed as an interpolation between a honeycomb lattice in graphene and a dice lattice characterized by a key structural parameter α which is a relative hub-rim hopping coefficient or a phase $\phi = \tan^{-1}\alpha$ related to the Berry phase of the lattice. Specifically, $\alpha = 0$ corresponds to graphene, whereas $\alpha = 1$ to a dice lattice. In reality, the most well-known examples of existing materials which fully

* E-mail contact: aiurov@mec.cuny.edu, theorist.physics@gmail.com

or partially resemble the α-$\mathcal{T}_3$ model in their electronic band structure include Lieb and Kagome optical lattices, [39–43] optical waveguides, [44,45] a trilayer $SrTiO_3/SrIrO_3/SrTiO_3$, [6] $Hg_{1-x}Cd_x$ quantum well, [46] Josephson-junction arrays [47] and $In_{0.53}Ga_{0.47}As/InP$ semiconducting layers [48]. A very informative and complete review of fabricated flat-band materials can be found in Ref. [4].

There have been a number of recent papers which discussed superconductivity in Kagome lattices. [49–51] Superconductivity has also been observed experimentally in graphene superlattices. [52,53] Additionally, induced superconductivity in regular graphene contacted by superconducting electrodes was reported in Ref. [54].

The energy band structure of α-$\mathcal{T}_3$ materials seems even more unusual in the presence of a finite bandgap. [55] In a general situation, two subbands, corresponding to valence and conduction bands, acquire non-equivalent gaps, and most importantly, the deformed flat band displays a curved shape. Interestingly, this deformed flat band now lies under the zero energy and reaches its maximum at $\boldsymbol{k} = 0$. Consequently, the only remaining materials with an unperturbed flat band are represented by two limiting cases, i.e. $\alpha = 0$ and $\alpha = 1$ corresponding to graphene and a dice lattice, respectively. Such a non-trivial bandgap, which affects all three bands of α-$\mathcal{T}_3$, will show up after applying an external off-resonance dressing field with a circular or an elliptical polarization. [17,56–58]

The low-energy states in $\alpha - \mathcal{T}_3$ model which belong to a Dirac cone (not the flat band) are chiral, similarly to the corresponding states in graphene. The band structure, which consists of the Dirac cone together with the flat band, does not describe the whole complexity of the system, but this approximation works fairly well for the low energies of electrons close to the Dirac cone.

The Dirac-cone approximation for the valence and conduction bands of $\alpha - \mathcal{T}_3$ materials is valid only within the same energy range as in graphene (up to $\backsim 7\,\mathrm{eV}$). Siimlarly, a real-life flat band cannot extend to infinite momenta. Mathematically, this simplified approximation lead to a very precise description for the actual band structure of $\alpha - \mathcal{T}_3$ materials as long as electron energy does not go beyond several times of Fermi energy ($\leq 10\,meV$). Correspondingly, our calculations for the optical conductivity remain valid in a similar frequency range.

It was demonstrated [59] that a finite anomalous Hall voltage could show up if a monolayer MoS_2 is irradiated by a light with a clockwise or counter-clockwise circular polarizations, which affects electrons differently in the $\boldsymbol{K}$ and $\boldsymbol{K}'$ valleys. Moreover, it was revealed [60,61] that the valley polarization and difference between quantum electronic states in two valleys of transition metal dichalcogenide monolayers, and how it is related to spin polarization, and applied laser irradiation with different helicities to further distinguish these two valleys, which could be used in quantum electronics. The important difference between MoS_2 (and other transition metal dichalcogenides) and graphene or $\alpha - \mathcal{T}_3$ model is that the energy dispersions in the latter cases do not directly depend on the valley index, which makes them less suitable for valleytronic applications.

The static conductivity for standard quantum transport is one of utmost importance and has extensively investigated properties of an interacting many-body electronic system. Semiclassically, if a current does not depend on the variation of random impurity positions, one can employ Boltzmann transport theory, which has been exemplified by studying various 2D materials. The temperature dependence involved in Boltzmann conductivity, resulting from phonon scattering of electrons, was also computed for graphene and other lattices. [62,63] Quantum-mechanically, on the other hand, the most general approach for calculating conductivity is based on Kubo formula, or more generally, a linear-response theory. For Kubo theory, its conductivity computation usually involves finding single-particle Green's functions and then the corresponding current-current (or velocity-velocity) correlation function.

The frequency-dependent optical conductivity is a fundamental electronic characteristics which was thoroughly investigated for novel low-dimensional materials, such as graphene, [64–66] silicene, [67,68] α-$\mathcal{T}_3$ and the dice lattice, [18,22,69] Kekule-patterned graphene, [70] transition-metal dichalcogenides, [71–74] 8-pmmn borophene [75,76] and twisted bilayers [77], even including a perpendicular quantizing magnetic field [9,35,78–80]. Yet, one important and very interesting issue on irradiated α-$\mathcal{T}_3$ having a curved middle band is still not addressed, which turns into the main subject of the present study. Here, the real part of the optical conductivity is related to absorption of photons, while its imaginary part determines the dielectric property of α-$\mathcal{T}_3$ material. As a 2D lattice is under an irradiation, the incident light could be absorbed through exciting an electron from its lower-energy state. Therefore, calculating the frequency dependence of the optical conductivity, one is able to provide valuable information on the electronic band energy structure of a target material, as well as the dipole-coupling strength of electron interband transitions between initial occupied and final empty states. Especially, a low-energy intraband transition across the Fermi level is responsible for well-known Drude conductivity. [1]

A vast experimental effort has already been put in to investigate the optical conductivity of all innovative two-dimensional Dirac materials starting from graphene [81,82] and a plenty of others. A very good agreement between experimental results and theoretical predictions was achieved. Therefore, we expect that our theoretical results for the optical conductivity of $\alpha - \mathcal{T}_3$ could also be confirmed experimentally in the near future.

Our calculation of optical conductivity did not include the self-energy of excited electrons in $\alpha-\mathcal{T}_3$. This is a leading-order approximation and a common practice in calculating optical conductivity of all previously known Dirac materials. In contrast, the self-energy must be taken into account in calculating optical conductivity of strongly-correlated systems, such as it was done in Refs. [83,84]. The effect of electron-electron interaction on the conductivity of graphene was taken into consideration using perturbation theory in an interaction parameter for the self energy. [85] Apart from that, an attempt to include self-energy into the model of a dc conductivity in a dice lattice in the presence of disorder was made in Ref. [86].

In this paper, we first review and discuss results for the band energy structure of α-$\mathcal{T}_3$ with a ϕ-dependent energy gap(s), as well as associated electronic states (wave functions) in Sec. II. Section III presents different techniques for calculating the optical conductivity of graphene or α-$\mathcal{T}_3$, which consists of finding electron Green's and spectral functions. Meanwhile, we also analyze and compare obtained results for the optical conductivity at zero and finite temperatures. The research summary, including both conclusion remarks and perspectives, is given in Sec. IV. For clarity, detailed calculations and derivations of single-electron states and their energy dispersions in the presence of a finite bandgap, expressions for Green's and spectral functions, and optical conductivities in a gapped dice lattice and an arbitrary α-$\mathcal{T}_3$ material are put in Appendices A, C and D, separately.

II. ELECTRONIC STATES WITH AN IRRADIATION-MODIFIED BANDSTRUCTURE

The optical conductivity depends on the electron band structure, or more specifically, on all possible transitions from an initial occupied to a final empty state of electrons in a material. Therefore, for completeness, we include calculating and analyzing non-trivial low-energy dispersions of a gapped α-$\mathcal{T}_3$ lattice. We begin with an overview of band energy dispersions and the corresponding eigenfunctions of the α-$\mathcal{T}_3$ model, which are obtained from a pseudospin-1 and ϕ-dependent Dirac-Weyl model Hamiltonian given by

$$\hat{\mathcal{H}}_\tau^\phi(\boldsymbol{k}) = \hbar v_F \begin{bmatrix} 0 & k_-^\tau \cos\phi & 0 \\ k_+^\tau \cos\phi & 0 & k_-^\tau \sin\phi \\ 0 & k_+^\tau \sin\phi & 0 \end{bmatrix}, \tag{1}$$

where $v_F = 10^6$ m/s is the Fermi velocity, the same as that for graphene to ensure the $\alpha \to 0$ limit of the α-$\mathcal{T}_3$ model, $\tau = \pm 1$ is the valley index, $\boldsymbol{k} = (k_x, k_y)$ is a wave vector and $k_\pm^\tau = \tau k_x \pm i k_y$. The expression for the Hamiltonian in Eq. (1) could be simplified as $\hat{\mathcal{H}}_\tau^\phi(\boldsymbol{k}) = \hbar v_F\, \hat{\boldsymbol{\Sigma}}(\phi)\cdot\boldsymbol{k}$ in terms of 3×3 and ϕ-dependent matrices $\hat{\Sigma}^{(3)}(\phi)$ listed and discussed in Appendi A.

The Hamiltonian in Eq. (1) yields three energy bands $\varepsilon_\gamma^{(0)}(\boldsymbol{k}) = \gamma\,\hbar v_F k$, corresponding to valence ($\gamma = -1$), conduction ($\gamma = +1$) and flat ($\gamma = 0$) bands. These energy bands are clearly independent of the parameters τ and ϕ. Moreover, the corresponding electronic eigenfunctions are

$$\Phi_0^{\gamma=\pm1}(\boldsymbol{k}|\,\tau,\phi) = \frac{1}{\sqrt{2}} \begin{bmatrix} \tau\cos\phi\ \mathsf{e}^{-i\tau\theta_{\mathbf{k}}} \\ \gamma \\ \tau\sin\phi\ \mathsf{e}^{i\tau\theta_{\mathbf{k}}} \end{bmatrix}, \tag{2}$$

where $\theta_{\mathbf{k}} = \arctan(k_y/k_x)$, and

$$\Phi_0^{\gamma=0}(\boldsymbol{k}|\,\tau,\phi) = \begin{bmatrix} \tau\sin\phi\ \mathsf{e}^{-i\tau\theta_{\mathbf{k}}} \\ 0 \\ -\tau\cos\phi\ \mathsf{e}^{i\tau\theta_{\mathbf{k}}} \end{bmatrix}. \tag{3}$$

For dressed states, however, their energy dispersion relations will rely on the Berry phase ϕ in contrast with the energy dispersion $\varepsilon_\gamma^{(0)}(\boldsymbol{k}) = \gamma\,\hbar v_F k$ of bare states.

The geometrical phase, which is also a Berry phase, is directly related to the phase $\phi = \tan^{-1}\alpha$. It represents one of the most important results for the $\alpha-\mathcal{T}_3$ model. As a rare occasion, it does depend on the phase ϕ or relative hopping parameter $\alpha = \tan\phi$ so that various $\alpha-\mathcal{T}_3$ materials could be distinguished from each other just by measuring their Berry phases.

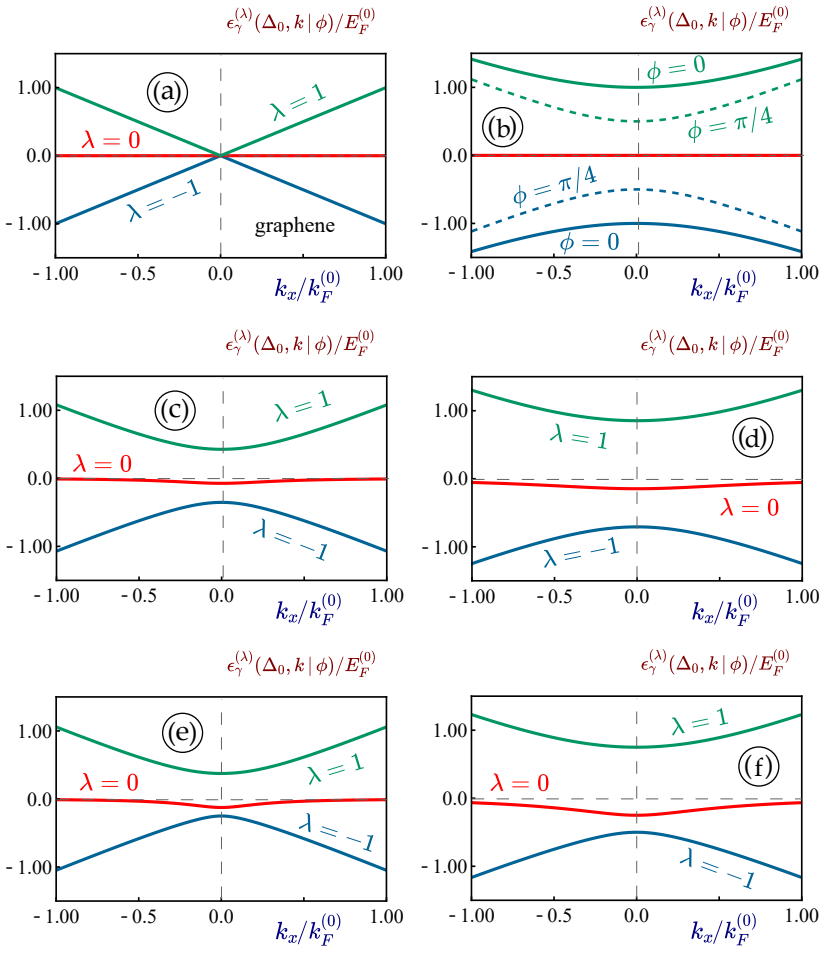

FIG. 1: (Color online) Energy dispersions $\varepsilon_\lambda(\Delta_0, \boldsymbol{k}\,|\,\phi)$ of various α-$\mathcal{T}_3$ materials in the presence of a finite energy gap Δ_0. Panel (a) demonstrates the dispersions of graphene and an arbitrary α-$\mathcal{T}_3$ lattice with a zero gap $\Delta_0 = 0$, plot (b) shows the energy subbands of graphene ($\phi = 0$, solid curves) and a dice lattice ($\phi = \pi/4$, dashed curves) with a finite bandgap $\Delta_0/E_F^{(0)} = 1$. Correspondingly, we set $\phi = \pi/8$ in panels (c) and (d) and $\phi = \pi/6$ in plots (e) and (f), respectively. As labeled, $\Delta_0 = 0$ for panel (a) and $\Delta_0/E_F^{(0)} = 0.5$ for panel (c) and (e), while $\Delta_0/E_F^{(0)} = 1$ in the right panels (b), (d) and (f).

Our main focus is, however, an α-$\mathcal{T}_3$ material in the presence of a finite bandgap Δ_0, and the previous Hamiltonian in Eq. (1) is generalized as

$$\hat{\mathcal{H}}_\tau^{(\phi)}(\boldsymbol{k}) \longrightarrow \hat{\mathcal{H}}_\tau^{(\phi)}(\boldsymbol{k}\,|\,\Delta_0) = \hat{\mathcal{H}}_\tau^{(\phi)}(\boldsymbol{k}) + \hat{\mathcal{H}}_a^{(\phi)}(\Delta_0)\ , \tag{4}$$

as employed in Ref. [87]. Here, the additional ϕ-dependent term $\hat{\mathcal{H}}_a^{(\phi)}(\Delta_0)$ in Eq. (4) takes the form

$$\hat{\mathcal{H}}_a^{(\phi)}(\Delta_0) = \frac{\Delta_0}{2}\,\hat{\Sigma}_z(\phi) = \Delta_0 \begin{bmatrix} \cos^2\phi & 0 & 0 \\ 0 & -\cos 2\phi & 0 \\ 0 & 0 & -\sin^2\phi \end{bmatrix}\ , \tag{5}$$

where $\hat{\Sigma}_z^{(\phi)} = -i\left[\hat{\Sigma}_x(\phi), \hat{\Sigma}_y(\phi)\right]$ is given and explained in Appendix A. On mathematical grounds, we find that such a Hamiltonian in Eq. (5) with an additional ϕ-dependent gap term is formally the same as one for an α-$\mathcal{T}_3$ material irradiated by a circularly-polarized dressing field to leading order. In the following, we will calculate the eigenenergies of the Hamiltonian in Eq. (4). But, even before we do this, it is already clear from Fig. 1 that two sub-gaps at $\boldsymbol{k} = 0$ are not equal and depend on the parameter α (or phase ϕ). Additionally, the middle band is no longer flat if $\phi \neq 0$ and $\phi \neq \pi/4$. The energy dispersion for gapped α-$\mathcal{T}_3$ determined by the Hamiltonian in Eq. (4) are found to be

$$\varepsilon_{\lambda}(k,\Delta_0\,|\,\phi) \;=\; \frac{2}{\sqrt{3}}\sqrt{\bar{k}^2+\frac{\Delta_0^2}{8}\left[5+3\cos(4\phi)\right]}\;\times \tag{6}$$
$$\times\;\cos\left\{\frac{2\pi(2+\lambda)}{3}+\frac{1}{3}\,\cos^{-1}\left(\frac{9\sqrt{6}\,\Delta_0^3\,\sin(2\phi)\,\sin(4\phi)}{\{8k^2+\Delta_0^2[5+3\cos(4\phi)]\}^{3/2}}\right)\right\}\;,$$

where $\lambda=0,\,\pm1$ specifies three different energy bands and $\bar{k}\equiv\hbar v_F k$.

For a small bandgap $\Delta_0\to 0$ and $k\neq 0$, the subbands given by Eq. (6) are reduced to

$$\varepsilon_{\lambda}(k,\Delta_0\ll k\,|\,\phi)=\frac{2}{\sqrt{3}}\left[\bar{k}+\frac{\Delta_0^2}{16\,\bar{k}}\,(5+3\cos 4\phi)\right]\left(\frac{\sqrt{3}\lambda}{2}+\frac{3\sqrt{3}\Delta_0^3}{32\bar{k}^3}\right)(2-|\lambda|)\,\sin(2\phi)\,\sin(4\phi)\;. \tag{7}$$

The energy dispersions in Eq. (6) and, especially, the bandgaps do not directly depend on τ, *i.e.*, all obtained results are valley degenerate. Meanwhile, we also find that obtained analytical expressions for optical conductivity of a gapped dice lattice and zero-gap $\alpha-\mathcal{T}_3$ materials, presented in Appendices C and D, do not demonstrate any explicit dependence on valley index τ.

Once the energy eigenvalues have been calculated, three components of a wave-function 3×1 column vector $\Psi_{\lambda}^{(j)}(k,\Delta_0\,|\,\phi)$ (with $j=1,\,2,\,3$), corresponding to each energy subband $\varepsilon_{\lambda}(k,\Delta_0\,|\,\phi)$, could be directly found from the eigenvalue equation of Hamiltonian in Eq. (4), leading to

$$\Psi_{\lambda}^{(1)}(\boldsymbol{k},\Delta_0\,|\,\phi) \;=\; \bar{k}\,\cos\phi\,\mathsf{e}^{-i\theta_{\mathbf{k}}}\,\left(\varepsilon_{\lambda}-\Delta_0\,\cos^2\phi\right)^{-1}\,\Psi_{\lambda}^{(2)}(\boldsymbol{k},\Delta_0\,|\,\phi)\;, \tag{8}$$
$$\Psi_{\lambda}^{(3)}(\boldsymbol{k},\Delta_0\,|\,\phi) \;=\; \bar{k}\,\sin\phi\,\mathsf{e}^{+i\theta_{\mathbf{k}}}\,\left(\varepsilon_{\lambda}+\Delta_0\,\sin^2\phi\right)^{-1}\,\Psi_{\lambda}^{(2)}(\boldsymbol{k},\Delta_0\,|\,\phi)\;, \tag{9}$$

where the remaining component $\Psi_{\lambda}^{(2)}(\boldsymbol{k},\Delta_0\,|\,\phi)$ in Eqs. (8) and (9) could be calculated explicitly from the normalization condition and expression for $\varepsilon_{\lambda}(k,\Delta_0\,|\,\phi)$ in Eq. (6) or Eq. (7), yielding

$$\Psi_{\lambda}^{(2)}(\boldsymbol{k},\Delta_0\,|\,\phi)=\left\{1+\left[\frac{\bar{k}\,\cos\phi}{(\varepsilon_{\lambda}+\Delta_0\,\cos^2\phi)}\right]^2+\left[\frac{\bar{k}\,\sin\phi}{(\varepsilon_{\lambda}+\Delta_0\,\sin^2\phi)}\right]^2\right\}^{-1/2}\;. \tag{10}$$

Relations in Eqs. (8) and (9) are not applicable and need modifications if both Δ_0 and ε_{λ} are zero. In this case, however, there exists a direct relation between $\Psi_{\lambda}^{(1)}(\boldsymbol{k},\Delta_0\,|\,\phi)$ and $\Psi_{\lambda}^{(3)}(\boldsymbol{k},\Delta_0\,|\,\phi)$. Similar results for energy dispersions and wave functions of gapped α-$\mathcal{T}_3$ have been presented in Refs. [87], [88]. Some details on the derivations of Eqs. (8)-(10) can be found in our Appendix A.

The calculated energy dispersion relations are displayed in Fig. 1, from which we clearly see that the middle band is indeed deformed and becomes curved once a finite bandgap Δ_0 is introduced. In addition, the middle band always lies below the zero energy and reaches its lowest point (negative peak) at $\boldsymbol{k}=0$. On the other hand, the valence and conduction band dispersions $\varepsilon_{\lambda}(k,\Delta_0\ll k\,|\,\phi)$ receive a non-uniform bandgap, which makes the whole band structure a lot more complex and gives rise to unique features in the optical conductivity. Furthermore, we find in Fig. 1 that the middle band returns to being to flat only in two limiting cases, i.e. graphene with $\phi=0$ and the dice lattice with $\phi=\pi/4$, as seen in Fig. 1(b).

Here, we emphasize that both energy dispersions and wave functions corresponding to different bands are expected to be crucial in computing the optical conductivity. Although the energies of allowed electronic states determine all possible electron transitions between an initial occupied and a final empty state, i.e. the energy range for which a nonzero optical conductivity exists, the wave function components in Eqs. (8)-(10) actually quantify the magnitude of the frequency dependence in the same optical conductivity.

III. OPTICAL CONDUCTIVITY

Once the electronic states and their energy dispersions are found, we arrive at a point to calculate the optical conductivity of α-$\mathcal{T}_3$ materials. By applying the Kubo formalism, the real (absorptive) part of the longitudinal conductivity $\sigma_{T}^{(\phi)}(\omega\,|\,\Delta_0)$ is given by

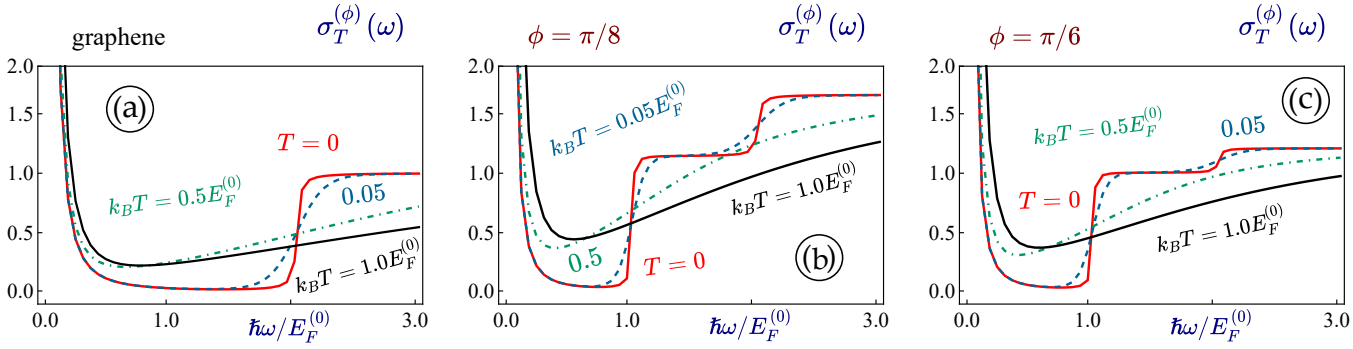

FIG. 2: (Color online) Temperature-dependent longitudinal optical conductivity $\sigma_T^{(\phi)}(\omega\,|\,\Delta_0=0)$ as a function of $\hbar\omega/\mu$ for graphene and different α-$\mathcal{T}_3$ materials with a finite chemical potential $\mu/E_F^{(0)}=1.0$ (or doped by electrons). Panel (a) shows the photon-frequency dependence $\hbar\omega/E_F^{(0)}$ of $\sigma_T^{(\phi)}(\omega\,|\,\Delta_0=0)$ for graphene with $\phi=0$. Plots (b) and (c) are for α-$\mathcal{T}_3$ materials with $\phi=\pi/8$ and $\phi=\pi/6$, respectively. Red-solid curves are used for zero-temperature results, blue-dashed ones for $k_BT/E_F^{(0)}=0.05$, green-dash-dotted ones for $k_BT/E_F^{(0)}=0.5$,and black-solid curves for $k_BT/E_F^{(0)}=1.0$ in each panel.

$$\sigma_T^{(\phi)}(\omega\,|\,\Delta_0)=\frac{\pi e^2}{\hbar}\int\frac{d\xi}{\hbar\omega}\,\mathbb{T}^{(\phi)}(\xi,\omega\,|\,\Delta_0)\,\left[n_F(\xi+\hbar\omega\,|\,\mu(T),T)-n_F(\xi\,|\,\mu(T),T)\right] \tag{11}$$

where we set $g_sg_e=4$ for the spin and valley degeneracy factors, $n_F(\xi\,|\,\mu,T)$ is the Fermi-Dirac distribution function, and $\mu(T)$ is the chemical potential such that $\mu(T)\longrightarrow E_F$ and $n_F(\xi\,|\,\mu,T)\longrightarrow\Theta(E_F-\xi)$ as $T\to0$. The detailed formalism for the optical conductivity calculation used in this Section is presented in Appendix B.

Another practical approach for calculating the optical conductivity of a two-dimensional lattice is based on finding a spectral function $\hat{\mathbb{S}}^{(\phi)}(\boldsymbol{k},\varepsilon\,|\,\Delta_0)$ which is related to the Green's function $\hat{\mathcal{G}}^{(\phi)}(\boldsymbol{k},\xi\,|\,\Delta_0)$ of an electron in a gapped α-$\mathcal{T}_3$ lattice through

$$\hat{\mathcal{G}}^{(\phi)}(\boldsymbol{k},\xi\,|\,\Delta_0)=\int\frac{d\varepsilon}{2\pi(\xi-\varepsilon)}\,\hat{\mathbb{S}}^{(\phi)}(\boldsymbol{k},\varepsilon\,|\,\Delta_0)\;. \tag{12}$$

Using this approach, we do not need express the velocity operators in the representation of a diagonalized Hamiltonian as seen in Eqs. (B4) and (B5). While these two approaches lead to the same results, computations of Green's function and spectral function of an α-$\mathcal{T}_3$ material, as well as a dice lattice, acquire some additional interests. [89]

The spectral functions $\hat{\mathbb{S}}^{(\phi)}(\boldsymbol{k},\varepsilon\,|\,\Delta_0)$ of a gapped dice lattice ($\phi=\pi/4$) and an arbitrary α-$\mathcal{T}_3$ material can be found from Appendices C and D, respectively. In fact, if elements of a Green's function can be decomposed into partial fractions, it is easy to use Eq. (12) by applying $1/(\xi-\varepsilon)\longrightarrow2\pi\,\delta(\xi-\varepsilon)$. However, such a partial-fraction decomposition is not nontrivial if a denominator represents a cubical equation. By utilizing the spectral function, the trace term in Eq. (B3) now becomes

$$\mathbb{T}^{(\phi)}(\xi,\omega\,|\,\Delta_0)=\int\frac{d^2\boldsymbol{k}}{2\pi}\,\mathrm{Tr}\left\{\hat{V}_x^{(\phi)}(\boldsymbol{k}\,|\,\Delta_0)\,\hat{\mathbb{S}}^{(\phi)}(\boldsymbol{k},\xi+\hbar\omega\,|\,\Delta_0)\,\hat{V}_x^{(\phi)}(\boldsymbol{k}\,|\,\Delta_0)\,\hat{\mathbb{S}}^{(\phi)}(\boldsymbol{k},\xi\,|\,\Delta_0)\right\}\;. \tag{13}$$

On the other hand, the Green's function for $\Delta_0=0$ is calculated explicitly as

$$\hat{\mathcal{G}}^{(\phi)}(\boldsymbol{k},\xi\,|\,\Delta_0=0)=\begin{bmatrix}\mathcal{G}^{(\phi)}_{1\,[1,0]}(k,\xi) & -\cos\phi\,\mathrm{e}^{-i\theta_{\boldsymbol{k}}}\,\mathcal{G}_2(k,\xi) & -\sin(2\phi)\,\mathrm{e}^{-2i\theta_{\boldsymbol{k}}}\,(k/2z)\,\mathcal{G}_2(k,\xi)\\ -\cos\phi\,\mathrm{e}^{i\theta_{\boldsymbol{k}}}\mathcal{G}_2(k,\xi) & \mathcal{G}_{1\,[0,1]}(k,\xi) & -\sin\phi\,\mathrm{e}^{-i\theta_{\boldsymbol{k}}}\,\mathcal{G}_2(k,\xi)\\ -\sin(2\phi)\,\mathrm{e}^{2i\theta_{\boldsymbol{k}}}\,(k/2z)\,\mathcal{G}_2(k,\xi) & -\sin\phi\,\mathrm{e}^{i\theta_{\boldsymbol{k}}}\,\mathcal{G}_2(k,\xi) & \mathcal{G}^{(\phi)}_{1\,[-1,1]}(k,\xi)\end{bmatrix}\;, \tag{14}$$

where we have defined notations

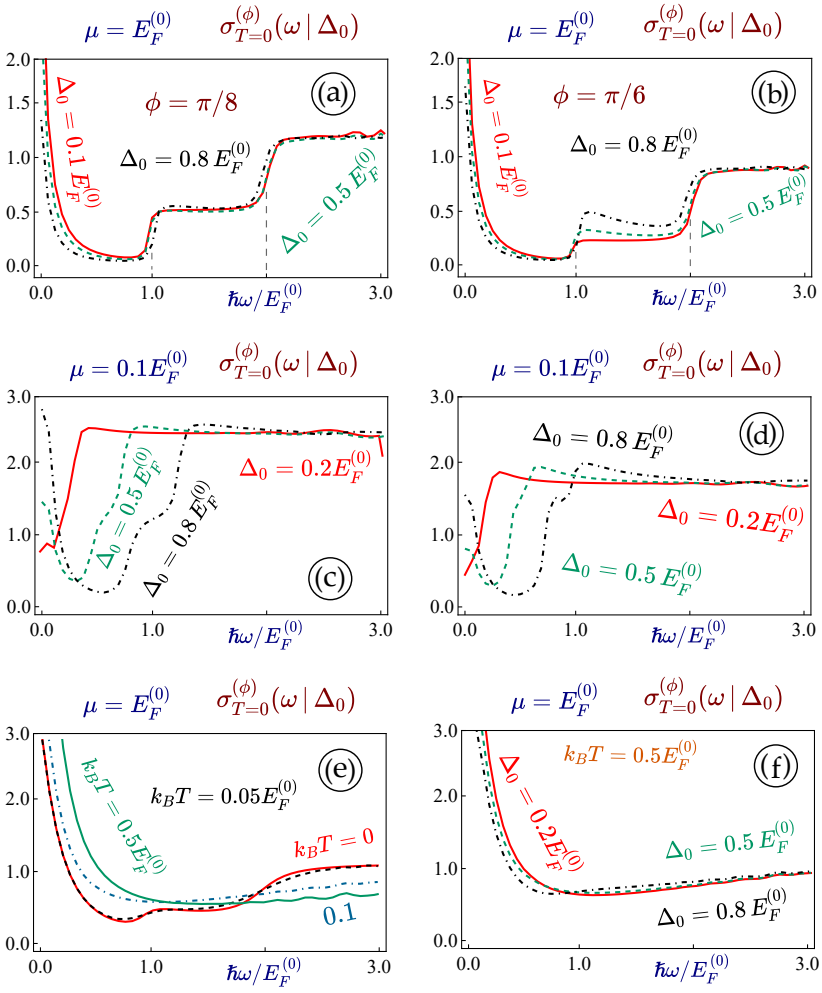

FIG. 3: (Color online) Longitudinal optical conductivity $\sigma_T^{(\phi)}(\omega\,|\,\Delta_0)$ for various α-$\mathcal{T}_3$ materials in the presence of a finite energy gap $\Delta_0 > 0$. Top panels (a) and (b), as well as bottom panels (e) and (f), correspond to $\mu/E_F^{(0)} = 1.0$, while middle panels (c) and (d) to nearly-zero doping $\mu/E_F^{(0)} = 0.1$ slightly above the middle band. Left panels (a) and (c) are for $\phi = \pi/8$, while right panels (b) and (d) for $\phi = \pi/6$. Finally, bottom panels (e) and (f) demonstrate $\sigma_T^{(\phi)}(\omega\,|\,\Delta_0)$ for gapped α-$\mathcal{T}_3$ materials having $\phi = \pi/6$ with different T in (e) and various Δ_0 in (f).

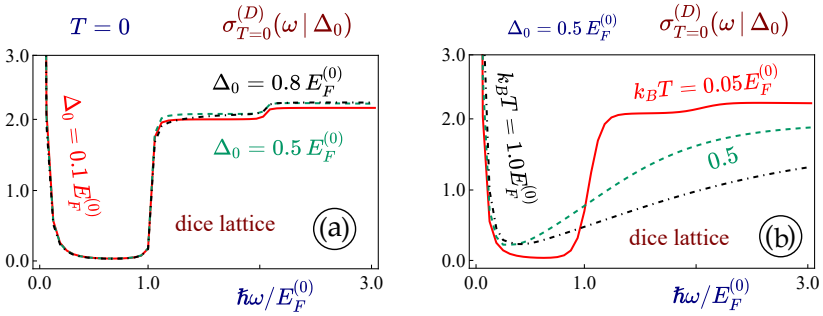

FIG. 4: (Color online) $\sigma_T^{(\phi)}(\omega\,|\,\Delta_0)$ for a dice lattice ($\phi = \pi/4$) at various T and with different Δ_0. Panel (a) displays $\sigma_T^{(\phi)}(\omega\,|\,\Delta_0)$ at $T = 0$ but with different Δ_0. Panel (b) shows $\sigma_T^{(\phi)}(\omega\,|\,\Delta_0)$ with a fixed $\Delta_0/E_F^{(0)} = 0.5$ but at various T. Here, red-solid curves represent the case of $k_BT/E_F^{(0)} = 0.05$, green-dashed curves the case of $k_BT = 0.5\,E_F^{(0)}$, black dash-dotted curves the case of $k_BT/E_F^{(0)} = 1.0$.

$$\mathcal{G}^{(\phi)}_{1\,[\beta,\nu]}(k,\xi) = \frac{\xi^2 + \beta\,\xi^2\,(\nu - \sin^2\phi)}{\xi^3 - \bar{k}^2\xi}\ ,$$
$$\mathcal{G}_2(k,\xi) = \frac{\bar{k}}{\xi^2 - \bar{k}^2}\ . \tag{15}$$

The current operator introduced in Eq. (B2) is $\hat{\mathbf{j}}^{\,(\phi)} = -e\hat{\mathbf{V}}^{\,(\phi)}$, and two velocity operatorsare

$$\hat{V}^{(\phi)}_x = v_F\,\hat{\Sigma}^{(\phi)}_x = v_F\begin{bmatrix} 0 & \cos\phi & 0 \\ \cos\phi & 0 & \sin\phi \\ 0 & \sin\phi & 0 \end{bmatrix} \tag{16}$$

and

$$\hat{V}^{(\phi)}_y = v_F\,\hat{\Sigma}^{(\phi)}_y = v_F\begin{bmatrix} 0 & -i\cos\phi & 0 \\ i\cos\phi & 0 & -i\sin\phi \\ 0 & i\sin\phi & 0 \end{bmatrix}\ , \tag{17}$$

which do not depend on the energy bandgap Δ_0, i.e., Eqs. (16) and (17) are the same for the cases of zero and a finite energy gap in α-$\mathcal{T}_3$.

The trace in Eq. (13) for a gapped dice lattice is given out in Appendix C, i.e.

$$\mathbb{T}^{\,(\phi)}(\xi,\omega\,|\,\Delta_0) = \frac{1}{2}\int\frac{d^2\boldsymbol{k}}{2\pi}\,\Big[\mathbb{T}^{(\phi)}_1(\boldsymbol{k},\xi,\omega\,|\,\Delta_0) + \mathbb{T}^{(\phi)}_2(k,\xi,\omega\,|\,\Delta_0)\Big]\ , \tag{18}$$

where

$$\begin{aligned}
\mathbb{T}^{(\phi)}_1(\boldsymbol{k},\xi,\omega\,|\,\Delta_0) &= \Big[\mathbb{S}^{(\phi)}_{21}(\boldsymbol{k},\xi\,|\,\Delta_0) + \mathbb{S}^{(\phi)}_{23}(\boldsymbol{k},\xi\,|\,\Delta_0)\Big]\ \Big[\mathbb{S}^{(\phi)}_{21}(\boldsymbol{k},\xi+\hbar\omega\,|\,\Delta_0) + \mathbb{S}^{(\phi)}_{23}(\boldsymbol{k},\xi+\hbar\omega\,|\,\Delta_0)\Big] \\
&+ \Big[\mathbb{S}^{(\phi)}_{12}(\boldsymbol{k},\xi\,|\,\Delta_0) + \mathbb{S}^{(\phi)}_{32}(\boldsymbol{k},\xi\,|\,\Delta_0)\Big]\ \Big[\mathbb{S}^{(\phi)}_{12}(\boldsymbol{k},\xi+\hbar\omega\,|\,\Delta_0) + \mathbb{S}^{(\phi)}_{32}(\boldsymbol{k},\xi+\hbar\omega\,|\,\Delta_0)\Big]\ , \\
\mathbb{T}^{(\phi)}_2(k,\xi,\omega\,|\,\Delta_0) &= \mathbb{S}^{(\phi)}_{22}(k,\xi+\hbar\omega\,|\,\Delta_0)\ \Big[\mathbb{S}^{(\phi)}_{11}(k,\xi\,|\,\Delta_0) + \mathbb{S}^{(\phi)}_{33}(k,\xi\,|\,\Delta_0)\Big] \\
&+ \mathbb{S}^{(\phi)}_{22}(k,\xi\,|\,\Delta_0)\ \Big[\mathbb{S}^{(\phi)}_{11}(k,\xi+\hbar\omega\,|\,\Delta_0) + \mathbb{S}^{(\phi)}_{33}(k,\xi+\hbar\omega\,|\,\Delta_0)\Big]\ .
\end{aligned} \tag{19}$$

Specifically, we look at the zero-gap limit of a dice lattice

$$\mathbb{T}^{\,(D)}(\xi,\omega\,|\,\Delta_0=0) = \int\frac{d^2\boldsymbol{k}}{4\pi}\,\Big[\mathbb{T}^{(D)}_1(k,\xi,\omega\,|\,\Delta_0=0) + \mathbb{T}^{(D)}_2(k,\xi,\omega\,|\,\Delta_0=0) + 4\,\mathbb{T}^{(D)}_3(k,\xi,\omega\,|\,\Delta_0=0)\Big]\ , \tag{20}$$

where

$$\begin{aligned}
\mathbb{T}^{(D)}_1(k,\xi,\omega\,|\,\Delta_0=0) &= \delta(\hbar\omega+\xi-\bar{k})\ \big[5\,\delta(\xi-\bar{k}) - 3\,\delta(\xi+\bar{k})\big]\ , \\
\mathbb{T}^{(D)}_2(k,\xi,\omega\,|\,\Delta_0=0) &= \delta(\hbar\omega+\xi+\bar{k})\ \big[5\,\delta(\xi+\bar{k}) - 3\,\delta(\xi-\bar{k})\big]\ , \\
\mathbb{T}^{(D)}_3(k,\xi,\omega\,|\,\Delta_0=0) &= \delta(\xi)\ \big[\delta(\xi+\hbar\omega-\bar{k}) + \delta(\xi+\hbar\omega+\bar{k})\big]\ .
\end{aligned} \tag{21}$$

Mathematically, however, we can write Eq. (21) into a more compact form, yielding

$$\mathbb{T}^{\,(D)}(\xi,\omega\,|\,\Delta_0=0) = \int\frac{d^2\boldsymbol{k}}{4\pi}\,\Big[\tilde{\mathbb{T}}^{(D)}_1(k,\xi,\omega\,|\,\Delta_0=0) + 4\,\tilde{\mathbb{T}}^{(D)}_3(k,\xi,\omega\,|\,\Delta_0=0)\Big]\ , \tag{22}$$

where

$$\tilde{\mathbb{T}}_1^{(D)}(k,\xi,\omega\,|\,\Delta_0=0)=\sum_{s=\pm1}\delta(\hbar\omega+\xi-s\bar{k})\,\left[5\,\delta(\xi-s\bar{k})-3\,\delta(\xi+s\bar{k})\right]\,, \tag{23}$$

$$\tilde{\mathbb{T}}_3^{(D)}(k,\xi,\omega\,|\,\Delta_0=0)=\delta(\xi)\sum_{s=\pm1}\delta(\xi+\hbar\omega+s\bar{k})\,.$$

For optical conductivity, we would like to point that the result in the $\Delta_0\longrightarrow 0$ limit of a dice lattice is the same as that of a graphene, as indicated at the end of Appendix D. Numerically, for our computation of an optical conductivity, we approx the delta function by a Lorentzian one, i.e.

$$\delta_\rho(x)=\frac{1}{\pi}\,\frac{\rho}{\rho^2+x^2} \tag{24}$$

with a small but yet a finite broadening parameter $\rho=0.01\,E_F^{(0)}$ in order to account for the impurity scattering $\backsim 2\rho$. This enables more realistic results for the optical conductivity.

The results in Fig. 2 for $\sigma_T^{(\phi)}(\omega\,|\,\Delta_0=0)$ of graphene and α-$\mathcal{T}_3$ without a bandgap display two jumps at $\hbar\omega/\mu=1$, 2 on the magnitudes of $\cos^2(2\phi)$ and $2\sin^2(2\phi)$, separately. All optical transitions below the Fermi level are blocked while those transitions in the range of $1<\hbar\omega/\mu<2$ are still allowed due to the presence of an occupied middle band. However, such limitations on electron transitions can still be lifted up by raising temperature T above zero. Here, the chemical potential $\mu(T)$ decreases from its maximum value (or Fermi energy $E_F^{(0)}$) at $T=0\,\mathrm{K}$ with increasing T. Our choice of $\mu(T)$ takes either $0.1\,E_F^{(0)}$ or $1.0\,E_F^{(0)}$, where $E_F^{(0)}=50\,\mathrm{meV}$ is a typical value for Fermi energy in graphene, corresponding to an electron sheet density $n_e=10^{11}\,\mathrm{cm}^{-2}$. Physically, the presence of an occupied middle band promotes electron transitions from it to the upper conduction band as $1<\hbar\omega/\mu<2$ and vice versa. The curvature of this middle band is solely determined by phase ϕ (or parameter α). Therefore, the magnitude ratio of the first over second jumps in $\sigma_T^{(\phi)}(\omega\,|\,\Delta_0=0)$ goes down as ϕ increases. Our focus of gapless α-$\mathcal{T}_3$ materials is on the T dependence in a gradual reduction of jump steps, as well as on the ω dependence of $\sigma_T^{(\phi)}(\omega\,|\,\Delta_0=0)$, in comparison with a standard case with a flat band.

Besides a phase ϕ-determined curved middle band, another key factor is the size of a bandgap Δ_0. The dependence of $\sigma_T^{(\phi)}(\omega\,|\,\Delta_0)$ on Δ_0 has been presented in Fig. 3 for various values of ϕ, T and μ. From Fig. 3, we easily find that the dominant two-step feature of $\sigma_T^{(\phi)}(\omega\,|\,\Delta_0)$ as a function of ω is largely retained even for $\mu/E_F^{(0)}=1$, $\phi=\pi/8$, $\pi/6$ and $T=0\,\mathrm{K}$. This main feature is found gradually washed out by increasing T and reducing μ. Smeared two-step appearance is also expected for $\mu/E_F^{(0)}\ll 1$ due to the fact that two steps will merge into one as μ approaches zero, which resembles the $\backsim\left(1-\Delta_0^2/\omega^2\right)$ dependence in zero-temperature optical conductivity of silicene with a finite spin-orbit gap. Therefore, for a gapped α-$\mathcal{T}_3$ at zero or finite temperatures, the main ω-characteristics in $\sigma_T^{(\phi)}(\omega\,|\,\Delta_0)$ looks qualitatively similar to each other for different values of Δ_0 at $\phi=\pi/8$, $\pi/6$, as can be verified from Figs. 3(a) and 3(f).

Surprisingly, a very special situation occurs as μ sits below the conduction band within the gap region, as presented in Fig. 3(c) and 3(d). In this case, the ω dependence of $\sigma_T^{(\phi)}(\omega\,|\,\Delta_0)$ does not show intraband Drude conductivity peak, i.e. $\backsim\delta(\omega)/\omega$ as $\omega\longrightarrow 0$, which shows up in all other cases. For an absent or a small bandgap, $\sigma_T^{(\phi)}(\omega\,|\,\Delta_0)$ remains nearly flat and becomes featureless, similarly to what was previously found in silicene. [1] Thus, the lowest frequency with a nonzero optical absorption is given by either μ or $2\Delta_0$, whichever is larger.

Fig. 3 (f) represents the case for an optical conductivity at an elevated temperature for which all sharp steps in optical conductivity are suppressed and smeared out over a wide frequency range due to change in the Fermi-Dirac distribution function. In such a situation, the ω dependence in $\sigma_T^{(\phi)}(\omega\,|\,\Delta_0=0)$ can no longer be substantial, and this is exactly what we find from the graph.

Finally, we look into the case of a gapped dice lattice ($\phi=\pi/4$) in which the flat band remains flat even if the valence and conduction bands receive a gap. Interestingly, at $T=0\,\mathrm{K}$ we only see one large Δ_0-independent jump of $\sigma_T^{(\phi)}(\omega\,|\,\Delta_0)$ at $\mu/E_F^{(0)}=1.0$ in Fig. 4(a). Meanwhile, apart from a weak second step, we see almost no dependence of $\sigma_T^{(\phi)}(\omega\,|\,\Delta_0)$ on ω above the Fermi level. Furthermore, we find that the dominant stepped structure in $\sigma_T^{(\phi)}(\omega\,|\,\Delta_0)$ is completely smeared out above $T=0\,\mathrm{K}$, as displayed in Fig. 4(b).

Our numerical results from Figs. 3 and 4 demonstrate that the dependence of optical conductivity on the bandgap becomes the most sensitive as ϕ stays far away from 0 and $\pi/4$. In these two limiting cases, however, the gap can

still affects the optical conductivity but the gap-induced shift of $\sigma_T^{(\phi)}(\omega \,|\, \Delta_0 = 0)$ with ω appears relatively uniform, which"includes the Drude peak $\delta(\omega)/\omega$ as $\omega \to 0$.

As far as the relevant phenomenology is concerned, one can propose an oversimplified model in which the optical conductivity consists only allowed electrons transitions. These transitions deal with those between an occupied and one free states which are solely determined by the energy band structure of material. This simple model suggests that we should still see two steps of a finite optical conductivity starting at both single and double Fermi energies due to the presence of a flat (or, nearly-flat) band. In the presence of a gap, one can speculate that these steps will receive additional peaks as seen in gapped graphene or silicene. However, our full-length calculations in this paper demonstrate that only one of two steps is strongly modified by this band gap. Different phenomenological descriptions of intraband transitions arise from Drude model and leads to an infinite peak $\backsimeq \delta(\omega)/\omega$ in the optical conductivity as $\omega \to 0$. This peak was verified in our calculations for all cases of optical conductivity with a finite doping.

IV. SUMMARY AND CONCLUDING REMARKS

In summary, we have calculated the optical conductivity for various kinds of gapped α-$\mathcal{T}_3$ materials in a wide range of temperature with different levels of electron doping. The calculated energy band structure of a gapped α-$\mathcal{T}_3$ lattice reveals several very unusual physical features except for the two limiting cases of graphene for $\phi = 0$ and a dice lattice with $\phi = \pi/4$, especially including a deformed (or curved) middle band. Therefore, the previous infinite degeneracy of a flat band has been fully split by this curvature, and then the Fermi level could be located at any point within its band width. Consequently, this curved middle band can now be doped either partially or fully. Such unusual energy dispersion relations and electronic states could be realized by introducing an off-resonance dressing field interacting with Dirac electrons in α-$\mathcal{T}_3$ materials.

We have found that the frequency-dependent optical conductivity shares all known features of those in zero-gap α-$\mathcal{T}_3$ materials as well as silicene with two inequivalent bandgaps. At zero temperature, the optical conductivity of graphene in the range of $\omega < 2\mu$ is zero because of Pauli blocking, meaning that carriers cannot transfer between two occupied states. For α-$\mathcal{T}_3$ materials, on the other hand, the same optical conductivity displays two successive steps corresponding to one transition between the valence and middle flat bands and another transition between the valence and conduction bands, separately. For electron doping, we further observe an infinite Drude conductivity peak $\backsim \delta(\omega)/\omega$ as $\omega \longrightarrow 0$ resulting from intraband transition of an electron with vanishing energy transfer between its initial and final states.

For a specific case with gapped α-$\mathcal{T}_3$ materials, only one of two jumps in optical conductivity displays a $\backsim \left(1 - \Delta_0^2/\omega^2\right)$ decrease which is absent for a dice lattice with only one such jump in optical conductivity at $\hbar\omega = \mu$. The dice lattice case is unique because the external irradiation field does not affect its flat band. Therefore, for this case, our computations are greatly simplified and analytical expressions for the Green's function, spectral weight and optical conductivity can be obtained. Meanwhile, we have derived analytical expressions for the zero-bandgap limit of a dice lattice, which is just the $\phi = \pi/4$ limit of a gapless α-$\mathcal{T}_3$ material. In addition, we have investigated the optical conductivity of both gapped and gapless α-$\mathcal{T}_3$ materials at finite temperatures.

Optical measurements are contactless in nature and become very useful in the quantitative analysis of the electronic band structure of a testing material. Experiments with respect to optical reflectivity, transmission and refraction enable ome to extract directly the dielectric function of the system, which is closely related to the band structure of a material. On the other hand, the same dielectric function is directly related to the optical conductivity of the system. Therefore, from an application perspective, optical conductivity is recognized as one of the most important measurable quantities, which has been thoroughly studied for many new low-dimensional materials. Its unique properties and, specifically, its frequency dependence allows for an experimental verification of the band structure of a target material with various doping levels. [90] We are confident that our discovery of unusual properties in this study for the optical conductivity of gapped α-$\mathcal{T}_3$ could be applied to a number of promising device applications, such as photodetectors, optical modulators and metasurfaces.

Acknowledgments

A.I. would like to acknowledge the funding received from TRADA-53-130, PSC-CUNY Award # 65094-00 53. D.H. was supported by the Air Force Office of Scientific Research (AFOSR). G.G. would like to acknowledge Grant No. FA9453-21-1-0046 from the Air Force Research Laboratory (AFRL).

Appendix A: Energy dispersions and wave functions for gapped α-$\mathcal{T}_3$

The Hamiltonian in Eq. (1) could be constructed by using the following two ϕ-dependent 3×3 matrices $\hat{\boldsymbol{S}}(\phi) = \left\{\hat{\Sigma}_x(\phi),\, \hat{\Sigma}_y(\phi)\right\}$, where

$$\hat{\Sigma}_x(\phi) = \begin{bmatrix} 0 & \cos\phi & 0 \\ \cos\phi & 0 & \sin\phi \\ 0 & \sin\phi & 0 \end{bmatrix} , \tag{A1}$$

and

$$\hat{\Sigma}_y(\phi) = i \begin{bmatrix} 0 & -\cos\phi & 0 \\ \cos\phi & 0 & -\sin\phi \\ 0 & \sin\phi & 0 \end{bmatrix} . \tag{A2}$$

Here, matrices in Eqs. (A1) and (A2) are ϕ-dependent generalization of 3×3 Pauli matrices defined by

$$\hat{\Sigma}_x^{(3)} = \frac{1}{\sqrt{2}} \begin{bmatrix} 0 & 1 & 0 \\ 1 & 0 & 1 \\ 0 & 1 & 0 \end{bmatrix} , \tag{A3}$$

$$\hat{\Sigma}_y^{(3)} = \frac{i}{\sqrt{2}} \begin{bmatrix} 0 & -1 & 0 \\ 1 & 0 & -1 \\ 0 & 1 & 0 \end{bmatrix} , \tag{A4}$$

which are related to a dice lattice by taking $\phi = \pi/4$ in Eqs. (A1) and (A2). On the other hand, as $\phi \to 0$, Eqs (A1) and (A2) reduce to regular spin-1/2 Pauli matrices used to describe the graphene Hamiltonian. Meanwhile, we also need to introduce the third Pauli matrix $\hat{\Sigma}_z^{(3)}$, defined as

$$\hat{\Sigma}_z^{(3)} = \begin{bmatrix} 1 & 0 & 0 \\ 0 & 0 & 0 \\ 0 & 0 & -1 \end{bmatrix} , \tag{A5}$$

in order to represent a gap term beyond the pseudospin-1 Hamiltonian in Eq. (1).

We will now calculate the eigenenergies of the Hamiltonian in Eq. (4). Before we proceed with that, it is noted that two gap values at $\boldsymbol{k} = 0$ depend on parameter α (or ϕ) and the middle band is no longer flat (or deformed). The sought energy dispersions are determined from the following secular equation

$$\left[\varepsilon(k, \Delta_0 \,|\, \phi)\right]^3 - c_1\, \varepsilon(k, \Delta_0 \,|\, \phi) - c_0 = 0 \, , \tag{A6}$$

where

$$c_1 = \bar{k}^2 + \frac{\Delta_0^2}{8} \left[5 + 3\cos(4\phi)\right] \, , \tag{A7a}$$

$$c_0 = \left(\frac{\Delta_0}{2}\right)^3 \sin(2\phi)\, \sin(4\phi) \, , \tag{A7b}$$

and $\bar{k} = \hbar v_F k$. From Eq. (A6), we see immediately the flat band (at $k = 0$) remains dispersionless if $c_0 = 0$, which is satisfied with either $\phi = 0$ or $\phi = \pi/4$, corresponding to two marginal cases of graphene and a dice lattice. For all other $0 < \phi < \pi/4$ (or $0 < \alpha < 1$), the flat band will be deformed (or become curved) in the presence of a finite bandgap $\Delta_0 \neq 0$.

Mathematically, Eq. (A6) is a *depressed cubical equation* with a missing $\backsim \varepsilon^2$ term. There is a number of ways to solve such type of equations. Being aware that there should be three real solutions to Eq. (A6), one of the best ways to find them is adopting Viete's formula in the form of trigonometric functions. Therefore, we start with rewriting Eq. (A6) to make it look similar to the following trigonometric identity

$$\cos^3\theta - \frac{3}{4}\,\cos\theta - \frac{1}{4}\,\cos(3\theta) = 0\ , \tag{A8}$$

or equivalently

$$\cos\theta\,\left[\cos^2\theta - \cos^2\left(\frac{\pi}{6}\right)\right] = \frac{1}{4}\,\cos(3\theta)\ , \tag{A9}$$

which is achieved by a substitution

$$\varepsilon(k,\Delta_0\,|\,\phi) = c_1^{1/2}\,\frac{\cos\theta}{\cos(\pi/6)}\ . \tag{A10}$$

As a result, from Eq. (A6) we find

$$\cos(3\theta) = 4\cos^3\left(\frac{\pi}{6}\right)\,\frac{c_0}{c_1^{3/2}}\ . \tag{A11}$$

Thus, from Eq. (A10) we obtain the energy eigenvalues

$$\varepsilon_\lambda(k,\Delta_0\,|\,\phi) = \frac{c_1^{1/2}}{\cos(\pi/6)}\,\cos\left\{\frac{2\pi\lambda}{3} + \frac{1}{3}\,\cos^{-1}\left[4\cos^3\left(\frac{\pi}{6}\right)\,\frac{c_0}{c_1^{3/2}}\right]\right\}\ , \tag{A12}$$

or explicitly

$$\begin{aligned}\varepsilon_\lambda^{(\phi)}(k,\Delta_0\,|\,\phi)\ &=\ \frac{2}{\sqrt{3}}\,\sqrt{\bar{k}^2 + \frac{\Delta_0^2}{8}\,(5+3\cos 4\phi)}\ \times \\ &\times\ \cos\left\{\frac{2\pi(2+\lambda)}{3} + \frac{1}{3}\,\cos^{-1}\left(\frac{9\sqrt{6}\,\Delta_0^3\,\sin 2\phi\,\sin 4\phi}{\left[8\bar{k}^2 + \Delta_0^2(5+3\cos(4\phi))\right]^{3/2}}\right)\right\}\ ,\end{aligned} \tag{A13}$$

where $\lambda = 0,\ 1,\ 2$ specifies three different energy bands. For a small bandgap $\Delta_0 \to 0$, subbands $\varepsilon_\lambda^{(\phi)}(k,\Delta_0 \ll k\,|\,\phi)$ in Eq. (A13) with $k \neq 0$ are simplified as

$$\begin{aligned}\varepsilon_\lambda(k,\Delta_0 \ll \bar{k}\,|\,\phi)\ &=\ \frac{2}{\sqrt{3}}\,\left[\bar{k} + \frac{\Delta_0^2}{16\,\bar{k}}\,(5+3\cos 4\phi)\right]\,\times \\ &\times\ \begin{cases}\sqrt{3}\lambda/2 + 3\sqrt{3}\Delta_0^3/(32\bar{k}^3)\cdot\sin(2\phi)\,\sin(4\phi)\ \ \text{for}\ \ \lambda = \pm 1\ , \\ 3\sqrt{3}\Delta_0^3/(16\bar{k}^3)\cdot\sin(2\phi)\,\sin(4\phi)\ \ \ \text{for}\ \ \lambda = 0\ .\end{cases}\end{aligned} \tag{A14}$$

Once the energy eigenvalues $\varepsilon_\lambda(k,\Delta_0\,|\,\phi)$ have been calculated, the wave-function components $\Psi_\lambda^{(j)}(\boldsymbol{k},\Delta_0\,|\,\phi)$ with $j = 1,2,3$ could be found in a relatively simple way, leading to

$$\Psi_\lambda^{(1)}(\boldsymbol{k},\Delta_0\,|\,\phi) = \bar{k}\,\cos\phi\,\mathsf{e}^{-i\theta_{\boldsymbol{k}}}\,\left[\varepsilon_\lambda(k,\Delta_0\,|\,\phi) - \Delta_0\,\cos^2\phi\right]^{-1}\,\Psi_\lambda^{(2)}(\boldsymbol{k},\Delta_0\,|\,\phi)\ , \tag{A15}$$

and

$$\Psi_{\lambda}^{(3)}(\boldsymbol{k},\Delta_0\,|\,\phi)=\bar{k}\,\sin\phi\,\mathsf{e}^{i\theta_{\mathbf{k}}}\,\left[\varepsilon_{\lambda}(k,\Delta_0\,|\,\phi)+\Delta_0\,\sin^2\phi\right]^{-1}\,\Psi_{\lambda}^{(2)}(\boldsymbol{k},\Delta_0\,|\,\phi)\;. \tag{A16}$$

The remaining component $\Psi_{\lambda}^{(2)}(\boldsymbol{k},\Delta_0\,|\,\phi)$ could be found from the normalization condition, yielding

$$\Psi_{\lambda}^{(2)}(\boldsymbol{k},\Delta_0\,|\,\phi)=\left\{1+\left[\frac{\bar{k}\,\cos\phi}{(\varepsilon_{\lambda}(k,\Delta_0\,|\,\phi)+\Delta_0\,\cos^2\phi)}\right]^2+\left[\frac{\bar{k}\,\sin\phi}{(\varepsilon_{\lambda}(k,\Delta_0\,|\,\phi)+\Delta_0\,\sin^2\phi)}\right]^2\right\}^{-1/2}\;. \tag{A17}$$

Relations in Eqs. (A15)-(A17) are not applicable and need modifications if both the bandgap Δ_0 and the energy eigenvalue $\varepsilon_{\lambda}(k,\Delta_0\,|\,\phi)$ are zero.

Appendix B: General formalism for optical conductivity

The most crucial dimensionless part in Eq. (11) is the trace of a product of four matrices, i.e.

$$\begin{aligned}\mathbb{T}^{\,(\phi)}(\xi,\omega\,|\,\Delta_0)\;&=\;\int\frac{d^2\boldsymbol{k}}{(2\pi)^2}\mathrm{Tr}\left\{\left[\hat{H}_{\tau}^{(\phi)}(\boldsymbol{k}\,|\,\Delta_0),x\right]\,\delta\left(\hat{H}_{\tau}^{(\phi)}(\boldsymbol{k}\,|\,\Delta_0)-\xi-\hbar\omega\right)\right.\\&\times\;\left.\left[\hat{H}_{\tau}^{(\phi)}(\boldsymbol{k}\,|\,\Delta_0),x\right]\,\delta\left(\hat{H}_{\tau}^{(\phi)}(\boldsymbol{k}\,|\,\Delta_0)-\xi\right)\right\}\;,\end{aligned} \tag{B1}$$

where by using the definition of an x-direction current operator $\hat{j}_x$, the operator $\left[\hat{H}_{\tau}^{(\phi)}(\boldsymbol{k}\,|\,\Delta_0),x\right]$ could be rewritten through the relation

$$\hat{j}_x^{\,(\phi)}=-i\,\frac{e}{\hbar}\left[\hat{H}_{\tau}^{(\phi)}(\boldsymbol{k}\,|\,\Delta_0),x\right]=-\frac{e}{\hbar}\frac{\partial\hat{H}_{\tau}^{(\phi)}(\boldsymbol{k}\,|\,\Delta_0)}{\partial k_x}\;, \tag{B2}$$

and a similar expression for the current $\hat{j}_y^{\,(\phi)}$ can be obtained in the same way. Since only isotropic materials and a circularly-polarized irradiation are concerned, we just calculate the $xx-$component of an optical conductivity. By substituting Eq. (B2) into Eq. (B1), we get

$$\mathbb{T}^{\,(\phi)}(\xi,\omega\,|\,\Delta_0)=\mathrm{Tr}\left\{\frac{\partial\hat{H}_{\tau}^{(\phi)}(\boldsymbol{k}\,|\,\Delta_0)}{\partial k_x}\,\delta\left(\hat{H}_{\tau}^{(\phi)}(\boldsymbol{k}\,|\,\Delta_0)-\xi-\hbar\omega\right)\,\frac{\partial\hat{H}_{\tau}^{(\phi)}(\boldsymbol{k}\,|\,\Delta_0)}{\partial k_x}\,\delta\left(\hat{H}_{\tau}^{(\phi)}(\boldsymbol{k}\,|\,\Delta_0)-\xi\right)\right\}\;. \tag{B3}$$

Equation (B3) can be evaluated in the representation in which the Hamiltonian $\hat{H}_{\tau}^{(\phi)}(\boldsymbol{k}\,|\,\Delta_0)$ becomes a diagonal matrix. For this reason, we introduce the following transformation, i.e.

$$\frac{\partial\hat{H}_{\tau}^{(\phi)}(\boldsymbol{k}\,|\,\Delta_0)}{\partial k_x}\;\longrightarrow\left\langle\hat{P}_{\psi}^{(-1)}(\boldsymbol{k},\Delta_0\,|\,\phi)\right|\frac{\partial\hat{H}_{\tau}^{(\phi)}(\boldsymbol{k}\,|\,\Delta_0)}{\partial k_x}\left|\hat{P}_{\psi}(\boldsymbol{k},\Delta_0\,|\,\phi)\right\rangle\;, \tag{B4}$$

and then we find

$$\begin{aligned}\delta\left(\hat{H}_{\tau}^{(\phi)}(\boldsymbol{k}\,|\,\Delta_0)-\xi\right)\;&\longrightarrow\;\left\langle\hat{P}_{\psi}^{(-1)}(\boldsymbol{k},\Delta_0\,|\,\phi)\right|\delta\left(\hat{H}_{\tau}^{(\phi)}(\boldsymbol{k}\,|\,\Delta_0)-\xi\right)\left|\hat{P}_{\psi}(\boldsymbol{k},\Delta_0\,|\,\phi)\right\rangle\\&=\;\begin{bmatrix}\delta\left(\epsilon_{\lambda=-1}(k,\Delta_0\,|\,\phi)-\xi\right)&0&0\\0&\delta\left(\epsilon_{\lambda=0}(k,\Delta_0\,|\,\phi)-\xi\right)&0\\0&0&\delta\left(\epsilon_{\lambda=+1}(k,\Delta_0\,|\,\phi)-\xi\right)\end{bmatrix}\;,\end{aligned} \tag{B5}$$

and $\left\langle\hat{P}_{\psi}^{(-1)}(\boldsymbol{k},\Delta_0\,|\,\phi)\right|\delta\left(\hat{H}_{\tau}^{(\phi)}(\boldsymbol{k}\,|\,\Delta_0)-\xi-\hbar\omega\right)\left|\hat{P}_{\psi}(\boldsymbol{k},\Delta_0\,|\,\phi)\right\rangle$ can be obtained in the same way. Here, the transformation matrix $\hat{P}_{\psi}(\boldsymbol{k},\Delta_0\,|\,\phi)$, initially introduced in Eq. (B4) for matrix diagonalization, can be built from the component of eigen-function defined in Eqs. (8)-(10), leading to

$$\hat{P}_{\psi}(\boldsymbol{k},\Delta_0\,|\,\phi)=\begin{bmatrix}\Psi^{(1)}_{\lambda=-1}(\boldsymbol{k},\Delta_0\,|\,\phi) & \Psi^{(1)}_{\lambda=0}(\boldsymbol{k},\Delta_0\,|\,\phi) & \Psi^{(1)}_{\lambda=+1}(\boldsymbol{k},\Delta_0\,|\,\phi)\\ \Psi^{(2)}_{\lambda=-1}(\boldsymbol{k},\Delta_0\,|\,\phi) & \Psi^{(2)}_{\lambda=0}(\boldsymbol{k},\Delta_0\,|\,\phi) & \Psi^{(2)}_{\lambda=+1}(\boldsymbol{k},\Delta_0\,|\,\phi)\\ \Psi^{(3)}_{\lambda=-1}(\boldsymbol{k},\Delta_0\,|\,\phi) & \Psi^{(3)}_{\lambda=0}(\boldsymbol{k},\Delta_0\,|\,\phi) & \Psi^{(3)}_{\lambda=+1}(\boldsymbol{k},\Delta_0\,|\,\phi)\end{bmatrix}. \tag{B6}$$

This transformation clearly does not change a trace of the product of four matrices $\hat{A}^{\,(\phi)}(\boldsymbol{k})\times\hat{\mathbb{O}}^{(\phi)}_{\xi}(\boldsymbol{k})\times\hat{A}^{\,(\phi)}(\boldsymbol{k})\times\hat{\mathbb{O}}^{(\phi)}_{\xi+\hbar\omega}(\boldsymbol{k})$ since

$$\begin{aligned}&\mathrm{Tr}\left\{\left[\hat{P}^{(-1)}_{\psi}\times\hat{A}\times\hat{P}_{\psi}\right]\times\left[\hat{P}^{(-1)}_{\psi}\times\hat{\mathbb{O}}_{\xi}\times\hat{P}_{\psi}\right]\times\left[\hat{P}^{(-1)}_{\psi}\times\hat{A}\times\hat{P}_{\psi}\right]\times\left[\hat{P}^{(-1)}_{\psi}\times\hat{\mathbb{O}}_{\xi+\hbar\omega}\times\hat{P}_{\psi}\right]\right\}\\ &=\mathrm{Tr}\left\{\hat{P}^{(-1)}_{\psi}\times\hat{A}\times\hat{\mathbb{O}}_{\xi}\times\hat{A}\times\hat{\mathbb{O}}_{\xi+\hbar\omega}\times\hat{P}_{\psi}\right\}\\ &=\mathrm{Tr}\left\{\hat{A}\times\hat{\mathbb{O}}_{\xi}\times\hat{A}\times\hat{\mathbb{O}}_{\xi+\hbar\omega}\times\hat{P}_{\psi}\times\hat{P}^{(-1)}_{\psi}\right\}=\mathrm{Tr}\left\{\hat{A}\times\hat{\mathbb{O}}_{\xi}\times\hat{A}\times\hat{\mathbb{O}}_{\xi+\hbar\omega}\right\},\end{aligned} \tag{B7}$$

where $\hat{A}^{\,(\phi)}(\boldsymbol{k})=\partial\hat{H}^{(\phi)}_{\tau}(\boldsymbol{k}\,|\,\Delta_0)/\partial k_x$, $\hat{\mathbb{O}}_{\xi}(\boldsymbol{k})=\delta\left(\hat{H}^{(\phi)}_{\tau}(\boldsymbol{k}\,|\,\Delta_0)-\xi\right)$ and $\hat{\mathbb{O}}_{\xi+\hbar\omega}(\boldsymbol{k})=\delta\left(\hat{H}^{(\phi)}_{\tau}(\boldsymbol{k}\,|\,\Delta_0)-\xi-\hbar\omega\right)$. Additionally, we also employ a well-know identity $\mathrm{Tr}\left\{\hat{A}\times\hat{B}\right\}=\mathrm{Tr}\left\{\hat{B}\times\hat{A}\right\}$.

For a gapless α-$\mathcal{T}_3$, the general transformation matrix in Eq. (B6) is simplified to

$$\hat{P}_{\psi}(\boldsymbol{k},\Delta_0=0\,|\,\phi)=\frac{1}{\sqrt{2}}\begin{bmatrix}\mathsf{e}^{-i\theta_{\mathbf{k}}}\cos\phi & \sqrt{2}\,\mathsf{e}^{-i\theta_{\mathbf{k}}}\sin\phi & \mathsf{e}^{-i\theta_{\mathbf{k}}}\cos\phi\\ 1 & 0 & -1\\ \mathsf{e}^{i\theta_{\mathbf{k}}}\sin\phi & \sqrt{2}\,\mathsf{e}^{i\theta_{\mathbf{k}}}\cos\phi & \mathsf{e}^{i\theta_{\mathbf{k}}}\sin\phi\end{bmatrix}, \tag{B8}$$

and further for graphene with $\phi=0$, it reduces to

$$\hat{P}_{\psi}(\boldsymbol{k},\Delta_0=0\,|\,\phi=0)=\frac{1}{\sqrt{2}}\begin{bmatrix}1 & 1\\ \mathsf{e}^{i\theta_{\mathbf{k}}} & -\mathsf{e}^{i\theta_{\mathbf{k}}}\end{bmatrix} \tag{B9}$$

which is a unitary matrix. This technique provides us with an analytical solution for calculating the trace in Eq. (B1), and then the optical conductivity in Eq. (11). For a gapped α-$\mathcal{T}_3$ material, however, the resulting expressions are too lengthy and complicated to write it down explicitly but this calculation approach is still very convenient and is often employed for numerical evaluation of $\sigma^{(\phi)}_{T=0}(\omega\,|\,\Delta_0)$ at zero temperature.

Appendix C: Green's functions and spectral functions for a gapped dice lattice.

The elements $\mathbb{S}^{(D)}_{ij}(k,\xi\,|\,\Delta_0)$ of a spectral function

$$\hat{\mathbb{S}}^{\,(D)}(\boldsymbol{k},\xi\,|\,\Delta_0)=\begin{bmatrix}\mathbb{S}^{(D)}_{11}(k,\xi\,|\,\Delta_0) & \mathbb{S}^{(D)}_{12}(\boldsymbol{k},\xi\,|\,\Delta_0) & \mathbb{S}^{(D)}_{13}(\boldsymbol{k},\xi\,|\,\Delta_0)\\ \mathbb{S}^{(D)}_{21}(\boldsymbol{k},\xi\,|\,\Delta_0) & \mathbb{S}^{(D)}_{22}(k,\xi\,|\,\Delta_0) & \mathbb{S}^{(D)}_{23}(\boldsymbol{k},\xi\,|\,\Delta_0)\\ \mathbb{S}^{(D)}_{31}(\boldsymbol{k},\xi\,|\,\Delta_0) & \mathbb{S}^{(D)}_{32}(\boldsymbol{k},\xi\,|\,\Delta_0) & \mathbb{S}^{(D)}_{33}(k,\xi\,|\,\Delta_0)\end{bmatrix} \tag{C1}$$

for a dice lattice ($\phi=\pi/4$) with a finite bandgap Δ_0 are calculated as

$$
\begin{aligned}
\mathbb{S}^{(D)}_{11}(k,\xi\,|\,\Delta_0)/\pi &= \left(\frac{\bar{k}}{\varepsilon_\Delta}\right)^2\delta(\xi)+\left[1-\frac{\bar{k}^2}{2\varepsilon_\Delta^2}+\frac{\Delta_0}{\varepsilon_\Delta}\right]\delta(\xi-\varepsilon_\Delta)+\left[1-\frac{\bar{k}^2}{2\varepsilon_\Delta^2}-\frac{\Delta_0}{\varepsilon_\Delta}\right]\delta(\xi+\varepsilon_\Delta)\;,\\
\mathbb{S}^{(D)}_{12}(\boldsymbol{k},\xi\,|\,\Delta_0)/\pi &= \frac{\bar{k}\,\mathsf{e}^{-i\theta_{\mathbf{k}}}}{\sqrt{2}}\left\{\left[\frac{1}{\varepsilon_\Delta}+\frac{\Delta_0}{2\varepsilon_\Delta^2}\right]\delta(\xi-\varepsilon_\Delta)+\left[-\frac{1}{\varepsilon_\Delta}+\frac{\Delta_0}{2\varepsilon_\Delta^2}\right]\delta(\xi+\varepsilon_\Delta)-\frac{\Delta_0}{\varepsilon_\Delta^2}\,\delta(\xi)\right\}\;,\\
\mathbb{S}^{(D)}_{21}(\boldsymbol{k},\xi\,|\,\Delta_0)/\pi &= \left[\mathbb{S}^{(D)}_{12}(\boldsymbol{k},\xi\,|\,\Delta_0)\right]^*/\pi\;,\\
\mathbb{S}^{(D)}_{13}(\boldsymbol{k},\xi\,|\,\Delta_0)/\pi &= \frac{\bar{k}^2\,\mathsf{e}^{-2i\theta_{\mathbf{k}}}}{2\varepsilon_\Delta^2}\times\left[\delta(\xi-\varepsilon_\Delta)+\delta(\xi+\varepsilon_\Delta)-2\,\delta(\xi)\right]\;,\\
\mathbb{S}^{(D)}_{31}(\boldsymbol{k},\xi\,|\,\Delta_0)/\pi &= \left[\mathbb{S}^{(D)}_{13}(\boldsymbol{k},\xi\,|\,\Delta_0)\right]^*/\pi\;,\\
\mathbb{S}^{(D)}_{22}(k,\xi\,|\,\Delta_0)/\pi &= \left(\frac{\Delta_0}{2\varepsilon_\Delta}\right)^2\delta(\xi)+\left[1-\left(\frac{\Delta_0}{2\varepsilon_\Delta}\right)^2\right]\left[\delta(\xi-\varepsilon_\Delta)+\delta(\xi+\varepsilon_\Delta)\right]\;,\\
\mathbb{S}^{(D)}_{23}(\boldsymbol{k},\xi\,|\,\Delta_0)/\pi &= \frac{\bar{k}\,\mathsf{e}^{-i\theta_{\mathbf{k}}}}{\sqrt{2}\,\varepsilon_\Delta^2}\left\{\Delta_0\,\delta(\xi)+\left[\varepsilon_\Delta-\frac{\Delta_0}{2}\right]\delta(\xi-\varepsilon_\Delta)-\left[\varepsilon_\Delta+\frac{\Delta_0}{2}\right]\delta(\xi+\varepsilon_\Delta)\right\}\;,\\
\mathbb{S}^{(D)}_{32}(\boldsymbol{k},\xi\,|\,\Delta_0)/\pi &= \left[\mathbb{S}^{(D)}_{23}(\boldsymbol{k},\xi\,|\,\Delta_0)/\pi\right]^*/\pi\;,\\
\mathbb{S}^{(D)}_{33}(k,\xi\,|\,\Delta_0)/\pi &= \left(\frac{\bar{k}}{\varepsilon_\Delta}\right)^2\delta(\xi)+\left[1-\frac{\bar{k}^2}{2\varepsilon_\Delta^2}-\frac{\Delta_0}{\varepsilon_\Delta}\right]\delta(\xi-\varepsilon_\Delta)+\left[1-\frac{\bar{k}^2}{2\varepsilon_\Delta^2}+\frac{\Delta_0}{\varepsilon_\Delta}\right]\delta(\xi+\varepsilon_\Delta)\;,
\end{aligned}
\tag{C2}
$$

where $\varepsilon_\Delta\equiv\varepsilon_\lambda(k,\Delta_0\,|\,\phi)$. For zero badngap $\Delta_0=0$, on the other hand, Eq. (C2) is simplified to

$$
\begin{aligned}
\mathbb{S}^{(D)}_{11}(k,\xi\,|\,\Delta_0=0)/\pi &= \delta(\xi)+[\delta(\xi-\bar{k})+\delta(\xi+\bar{k})]/2\;,\\
\mathbb{S}^{(D)}_{12}(k,\xi\,|\,\Delta_0=0)/\pi &= \mathsf{e}^{-i\theta_{\mathbf{k}}}\,\left[\delta(\xi-\bar{k})-\delta(\xi+\bar{k})\right]/\sqrt{2}\;,\\
\mathbb{S}^{(D)}_{21}(k,\xi\,|\,\Delta_0=0)/\pi &= \left[\mathbb{S}^{(D)}_{12}(k,\xi\,|\,\Delta_0=0)\right]^*/\pi\;,\\
\mathbb{S}^{(D)}_{13}(k,\xi\,|\,\Delta_0=0)/\pi &= \mathsf{e}^{-2i\theta_{\mathbf{k}}}\,\left[\delta(\xi+\bar{k})+\delta(\xi-\bar{k})-2\,\delta(\xi)\right]/2\;,\\
\mathbb{S}^{(D)}_{31}(k,\xi\,|\,\Delta_0=0)/\pi &= \left[\mathbb{S}^{(D)}_{13}(k,\xi\,|\,\Delta_0=0)\right]^*/\pi\;,\\
\mathbb{S}^{(D)}_{22}(k,\xi\,|\,\Delta_0=0)/\pi &= \delta(\xi-\bar{k})+\delta(\xi+\bar{k})\,,\\
\mathbb{S}^{(D)}_{23}(k,\xi\,|\,\Delta_0=0)/\pi &= \mathsf{e}^{-i\theta_{\mathbf{k}}}\,\left[\delta(\xi-\bar{k})-\delta(\xi+\bar{k})\right]/\sqrt{2}\;,\\
\mathbb{S}^{(D)}_{32}(k,\xi\,|\,\Delta_0=0)/\pi &= \left[\mathbb{S}^{(D)}_{23}(k,\xi\,|\,\Delta_0=0)\right]^*/\pi\;,\\
\mathbb{S}^{(D)}_{33}(k,\xi\,|\,\Delta_0=0)/\pi &= \delta(\xi)+[\delta(\xi-\bar{k})+\delta(\xi+\bar{k})]/2\;.
\end{aligned}
\tag{C3}
$$

Finally, by making use of results in Eqs. (C2) for a gapped dice lattice, the sought trace $\mathbb{T}^{(D)}(\xi,\omega\,|\,\Delta_0)$ takes the explicit form

$$
\mathbb{T}^{(D)}(\xi,\omega\,|\,\Delta_0)=\frac{1}{2}\int\frac{d^2\boldsymbol{k}}{2\pi}\,\left[\mathbb{T}^{(D)}_1(\boldsymbol{k},\xi,\omega\,|\,\Delta_0)+\,\mathbb{T}^{(D)}_2(\boldsymbol{k},\xi,\omega\,|\,\Delta_0)\right]\;,
\tag{C4}
$$

where

$$
\begin{aligned}
\mathbb{T}^{(D)}_1(\boldsymbol{k},\xi,\omega\,|\,\Delta_0) &= \left[\mathbb{S}^{(D)}_{21}(\boldsymbol{k},\xi\,|\,\Delta_0)+\mathbb{S}^{(D)}_{23}(\boldsymbol{k},\xi\,|\,\Delta_0)\right]\,\left[\mathbb{S}^{(D)}_{21}(\boldsymbol{k},\xi+\hbar\omega\,|\,\Delta_0)+\mathbb{S}^{(D)}_{23}(\boldsymbol{k},\xi+\hbar\omega\,|\,\Delta_0)\right]\\
&+\left[\mathbb{S}^{(D)}_{12}(\boldsymbol{k},\xi\,|\,\Delta_0)+\mathbb{S}^{(D)}_{32}(\boldsymbol{k},\xi\,|\,\Delta_0)\right]\,\left[\mathbb{S}^{(D)}_{12}(\boldsymbol{k},\xi+\hbar\omega\,|\,\Delta_0)+\mathbb{S}^{(D)}_{32}(\boldsymbol{k},\xi+\hbar\omega\,|\,\Delta_0)\right]\\
\mathbb{T}^{(D)}_2(\boldsymbol{k},\xi,\omega\,|\,\Delta_0) &= \mathbb{S}^{(D)}_{22}(\boldsymbol{k},\xi+\hbar\omega\,|\,\Delta_0)\,\left[\mathbb{S}^{(D)}_{11}(\boldsymbol{k},\xi\,|\,\Delta_0)+\mathbb{S}^{(D)}_{33}(\boldsymbol{k},\xi\,|\,\Delta_0)\right]\\
&+\mathbb{S}^{(D)}_{22}(\boldsymbol{k},\xi\,|\,\Delta_0)\,\left[\mathbb{S}^{(D)}_{11}(\boldsymbol{k},\xi+\hbar\omega\,|\,\Delta_0)+\mathbb{S}^{(D)}_{33}(\boldsymbol{k},\xi+\hbar\omega\,|\,\Delta_0)\right]\;.
\end{aligned}
\tag{C5}
$$

In particular, for $\Delta_0 = 0$, we find from Eqs. (C4) and (C5) that

$$\mathbb{T}^{(D)}(\xi,\omega\,|\,\Delta_0=0) = \int \frac{d^2\boldsymbol{k}}{4\pi}\,\left[\mathbb{T}_1^{(D)}(k,\xi,\omega\,|\,\Delta_0=0) + \mathbb{T}_2^{(D)}(k,\xi,\omega\,|\,\Delta_0=0) + 4\,\mathbb{T}_3^{(D)}(k,\xi,\omega\,|\,\Delta_0=0)\right]\,, \tag{C6}$$

where

$$\begin{aligned}
\mathbb{T}_1^{(D)}(k,\xi,\omega\,|\,\Delta_0=0) &= \delta(\hbar\omega+\xi-\bar{k})\,\left[5\,\delta(\xi-\bar{k}) - 3\,\delta(\xi+\bar{k})\right]\,,\\
\mathbb{T}_2^{(D)}(k,\xi,\omega\,|\,\Delta_0=0) &= \delta(\hbar\omega+\xi+\bar{k})\,\left[5\,\delta(\xi+\bar{k}) - 3\,\delta(\xi-\bar{k})\right]\,,\\
\mathbb{T}_3^{(D)}(k,\xi,\omega\,|\,\Delta_0=0) &= \delta(\xi)\,\left[\delta(\xi+\hbar\omega-\bar{k}) + \delta(\xi+\hbar\omega+\bar{k})\right]\,.
\end{aligned} \tag{C7}$$

In fact, we can rewrite Eqs. (C6) and (C7) in a more compact form, giving rise to

$$\mathbb{T}^{(D)}(\xi,\omega\,|\,\Delta_0=0) = \int \frac{d^2\boldsymbol{k}}{4\pi}\,\left[\tilde{\mathbb{T}}_1^{(D)}(k,\xi,\omega\,|\,\Delta_0=0) + 4\,\tilde{\mathbb{T}}_3^{(D)}(k,\xi,\omega\,|\,\Delta_0=0)\right]\,, \tag{C8}$$

where

$$\begin{aligned}
\tilde{\mathbb{T}}_1^{(D)}(k,\xi,\omega\,|\,\Delta_0=0) &= \sum_{s=\pm1}\delta(\hbar\omega+\xi-\bar{k})\,\left[5\,\delta(\xi-s\bar{k}) - 3\,\delta(\xi+s\bar{k})\right]\,,\\
\tilde{\mathbb{T}}_3^{(D)}(k,\xi,\omega\,|\,\Delta_0=0) &= \delta(\xi)\,\sum_{s=\pm1}\delta(\xi+\hbar\omega+s\bar{k})\,.
\end{aligned} \tag{C9}$$

Appendix D: Green's functions and spectral functions for gapless α-$\mathcal{T}_3$ model

For a general case, the spectral function can be written as

$$\hat{\mathbb{S}}^{(\phi)}(k,\xi) = \begin{bmatrix} \mathbb{S}_{11}^{(\phi)}(k,\xi) & \mathbb{S}_{12}^{(\phi)}(\boldsymbol{k},\xi) & \mathbb{S}_{13}^{(\phi)}(\boldsymbol{k},\xi)\\ \mathbb{S}_{21}^{(\phi)}(\boldsymbol{k},\xi) & \mathbb{S}_{22}^{(\phi)}(k,\xi) & \mathbb{S}_{23}^{(\phi)}(\boldsymbol{k},\xi)\\ \mathbb{S}_{31}^{(\phi)}(\boldsymbol{k},\xi) & \mathbb{S}_{32}^{(\phi)}(\boldsymbol{k},\xi) & \mathbb{S}_{33}^{(\phi)}(k,\xi)\end{bmatrix}\,, \tag{D1}$$

where its matrix elements for an arbitrary α-$\mathcal{T}_3$ are given by

$$\begin{aligned}
\mathbb{S}_{11}^{(\phi)}(k,\xi)/\pi &= \cos^2\phi\,\left[\delta(\xi-\bar{k}) + \delta(\xi+\bar{k})\right] + 2\,\sin^2\phi\,\delta(\xi)\,,\\
\mathbb{S}_{12}^{(\phi)}(\boldsymbol{k},\xi)/\pi &= \mathsf{e}^{-i\theta_{\mathbf{k}}}\,\cos\phi\,\left[\delta(\xi-\bar{k}) - \delta(\xi+\bar{k})\right]\,,\\
\mathbb{S}_{21}^{(\phi)}(\boldsymbol{k},\xi)/\pi &= \left[\mathbb{S}_{12}^{(\phi)}(\boldsymbol{k},\xi)/\pi\right]^* = \mathsf{e}^{i\theta_{\mathbf{k}}}\,\cos\phi\,\left[\delta(\xi-\bar{k}) - \delta(\xi+\bar{k})\right]\,,\\
\mathbb{S}_{13}^{(\phi)}(\boldsymbol{k},\xi)/\pi &= \mathsf{e}^{-2i\theta_{\mathbf{k}}}\,\sin(2\phi)\,\left[-\frac{1}{2}\,\delta(\xi) + \delta(\xi-\bar{k}) + \delta(\xi+\bar{k})\right]\,,\\
\mathbb{S}_{31}^{(\phi)}(\boldsymbol{k},\xi)/\pi &= \left[\mathbb{S}_{13}^{(\phi)}(\boldsymbol{k},\xi)/\pi\right]^* = \mathsf{e}^{2i\theta_{\mathbf{k}}}\,\sin(2\phi)\,\left[\delta(\xi-\bar{k}) + \delta(\xi+\bar{k}) - \frac{1}{2}\,\delta(\xi)\right]\,,\\
\mathbb{S}_{22}^{(\phi)}(k,\xi)/\pi &= \delta(\xi-\bar{k}) + \delta(\xi+\bar{k})\,,\\
\mathbb{S}_{23}^{(\phi)}(\boldsymbol{k},\xi)/\pi &= \mathsf{e}^{-i\theta_{\mathbf{k}}}\,\sin\phi\,\left[\delta(\xi-\bar{k}) - \delta(\xi+\bar{k})\right]\,,\\
\mathbb{S}_{32}^{(\phi)}(\boldsymbol{k},\xi)/\pi &= \left[\mathbb{S}_{23}^{(\phi)}(\boldsymbol{k},\xi)/\pi\right]^* = \mathsf{e}^{i\theta_{\mathbf{k}}}\,\sin\phi\,\left[\delta(\xi-\bar{k}) - \delta(\xi+\bar{k})\right]\,,\\
\mathbb{S}_{33}^{(\phi)}(k,\xi)/\pi &= \sin^2\phi\,\left[\delta(\xi-\bar{k}) + \delta(\xi+\bar{k})\right] + 2\,\cos^2\phi\,\delta(\xi)\,.
\end{aligned} \tag{D2}$$

Consequently, the trace in Eq. (B3) becomes

$$\mathbb{T}^{(\phi)}(\xi,\omega) = \int \frac{d^2\boldsymbol{k}}{4\pi}\,\left[\mathbb{T}_1^{(\phi)}(k,\xi\,|\,\omega)\,\cos^2\phi + \frac{1}{2}\,\mathbb{T}_2^{(\phi)}(\boldsymbol{k},\xi\,|\,\omega)\,\sin(2\phi) + \mathbb{T}_3^{(\phi)}(k,\xi\,|\,\omega)\,\sin^2\phi\right]\,, \tag{D3}$$

where

$$\begin{aligned}
\mathbb{T}_1^{(\phi)}(k,\xi\,|\,\omega) &= \mathbb{S}_{11}^{(\phi)}(k,\xi+\hbar\omega)\,\mathbb{S}_{22}^{(\phi)}(k,\xi) + \mathbb{S}_{11}^{(\phi)}(k,\xi)\,\mathbb{S}_{22}^{(\phi)}(k,\xi+\hbar\omega)\,, \\
\mathbb{T}_2^{(\phi)}(\boldsymbol{k},\xi\,|\,\omega) &= \sum_{\nu=\pm1}\left\{\mathbb{S}_{21}^{(\phi)}\left[\boldsymbol{k},\xi+(\nu+1)\,\frac{\hbar\omega}{2}\right]\,\mathbb{S}_{23}^{(\phi)}\left[\boldsymbol{k},\xi+(\nu+1)\,\frac{\hbar\omega}{2}\right]\right. \\
&+ \left.\mathbb{S}_{11}^{(\phi)}\left[k,\xi+(\nu+1)\,\frac{\hbar\omega}{2}\right]\,\mathbb{S}_{12}^{(\phi)}\left[\boldsymbol{k},\xi+(\nu+1)\,\frac{\hbar\omega}{2}\right]\right\} \\
&+ \sum_{\nu=\pm1}\mathbb{S}_{22}^{(\phi)}\left[k,\xi+(\nu+1)\,\frac{\hbar\omega}{2}\right]\left\{\mathbb{S}_{13}^{(\phi)}\left[\boldsymbol{k},\xi+(\nu+1)\,\frac{\hbar\omega}{2}\right] + \mathbb{S}_{31}^{(\phi)}\left[\boldsymbol{k},\xi+(\nu+1)\,\frac{\hbar\omega}{2}\right]\right\}\,, \qquad \text{(D4)} \\
\mathbb{T}_3^{(\phi)}(k,\xi\,|\,\omega) &= \mathbb{S}_{22}^{(\phi)}(k,\xi+\hbar\omega)\,\mathbb{S}_{33}^{(\phi)}(k,\xi) + \mathbb{S}_{22}^{(\phi)}(k,\xi)\,\mathbb{S}_{33}^{(\phi)}(k,\xi+\hbar\omega)\,. \qquad \text{(D5)}
\end{aligned}$$

In Eq. (D4), we have preliminary excluded terms with a angular dependence $\backsim \mathsf{e}^{\pm 2i\theta_{\boldsymbol{k}}}$, $\backsim \mathsf{e}^{\pm 3i\theta_{\boldsymbol{k}}}$ and $\backsim \mathsf{e}^{\pm 4i\theta_{\boldsymbol{k}}}$, which become zero after the angular integration in Eq. (D2) has been performed. It is easy to see that the last term of $\mathbb{T}_2^{(\phi)}(\boldsymbol{k},\xi\,|\,\omega)$ equals to zero for all $\phi \neq \pi/4$ (except for a dice lattice). Especially, for graphene with $\phi = 0$, we get the familiar result, i.e.

$$\begin{aligned}
\mathbb{T}^{(G)}(\xi,\omega) &= \int \frac{d^2\boldsymbol{k}}{4\pi}\,\left[\mathbb{S}_{11}^{(G)}(k,\xi+\hbar\omega)\,\mathbb{S}_{22}^{(G)}(k,\xi) + \mathbb{S}_{11}^{(G)}(k,\xi)\,\mathbb{S}_{22}^{(G)}(k,\xi+\hbar\omega)\right] \\
&= \int \frac{d^2\boldsymbol{k}}{2\pi}\,\left[\delta(\xi-\bar{k})+\delta(\xi+\bar{k})\right]\,\left[\delta(\xi-\bar{k}+\hbar\omega)+\delta(\xi+\bar{k}+\hbar\omega)\right]\,.
\end{aligned} \tag{D6}$$

Moreover, for another limit of a gapless dice lattice with $\phi = \pi/4$ and $\Delta_0 = 0$, we are able to get the same results as those in previous Appendix C.

[1] C. Tabert, Ph.D. thesis, University of Guelph (2015).
[2] E. Illes, Ph.D. thesis, University of Guelph (2017).
[3] D. Bercioux, D. Urban, H. Grabert, and W. Häusler, Physical Review A **80**, 063603 (2009).
[4] D. Leykam, A. Andreanov, and S. Flach, Advances in Physics: X **3**, 1473052 (2018).
[5] A. Raoux, M. Morigi, J.-N. Fuchs, F. Piéchon, and G. Montambaux, Physical review letters **112**, 026402 (2014).
[6] F. Wang and Y. Ran, Physical Review B **84**, 241103 (2011).
[7] E. Gorbar, V. Gusynin, and D. Oriekhov, Physical Review B **99**, 155124 (2019).
[8] A. Iurov, L. Zhemchuzhna, G. Gumbs, D. Huang, D. Dahal, and Y. Abranyos, Phys. Rev. B **105**, 245414 (2022).
[9] T. Biswas and T. K. Ghosh, Journal of Physics: Condensed Matter **30**, 075301 (2018).
[10] F. Li, Q. Zhang, and K. S. Chan, Scientific Reports **12**, 1 (2022).
[11] A. Filusch, A. R. Bishop, A. Saxena, G. Wellein, and H. Fehske, Physical Review B **103**, 165114 (2021).
[12] X. Zhou, Physical Review B **104**, 125441 (2021).
[13] S. F. Islam and P. Dutta, Physical Review B **96**, 045418 (2017).
[14] A. Balassis, D. Dahal, G. Gumbs, A. Iurov, D. Huang, and O. Roslyak, Journal of Physics: Condensed Matter **32**, 485301 (2020).
[15] E. Illes and E. Nicol, Physical Review B **94**, 125435 (2016).
[16] B. Dey and T. K. Ghosh, Physical Review B **98**, 075422 (2018).
[17] A. Iurov, G. Gumbs, and D. Huang, Physical Review B **99**, 205135 (2019).
[18] E. Illes, J. Carbotte, and E. Nicol, Physical Review B **92**, 245410 (2015).
[19] K. R. Bryenton, Ph.D. thesis, University of Guelph (2018).
[20] A. Iurov, L. Zhemchuzhna, G. Gumbs, D. Huang, and P. Fekete, Physical Review B **105**, 115309 (2022).
[21] J. Wang, J. Liu, and C. Ting, Physical Review B **101**, 205420 (2020).
[22] Á. D. Kovács, G. Dávid, B. Dóra, and J. Cserti, Physical Review B **95**, 035414 (2017).
[23] E. Illes and E. Nicol, Physical Review B **95**, 235432 (2017).
[24] A. Iurov, L. Zhemchuzhna, P. Fekete, G. Gumbs, and D. Huang, Physical Review Research **2**, 043245 (2020).

[25] X. Ye, S.-S. Ke, X.-W. Du, Y. Guo, and H.-F. Lü, Journal of Low Temperature Physics **199**, 1332 (2020).
[26] S. Cunha, D. da Costa, J. M. Pereira Jr, R. Costa Filho, B. Van Duppen, and F. Peeters, Physical Review B **105**, 165402 (2022).
[27] A. Korol, A. Sokolenko, and O. Shevchenko, Low Temperature Physics **47**, 300 (2021).
[28] L. Mandhour and F. Bouhadida, arXiv preprint arXiv:2004.10144 (2020).
[29] J. Malcolm and E. Nicol, Physical Review B **93**, 165433 (2016).
[30] A. Iurov, G. Gumbs, and D. Huang, Journal of Physics: Condensed Matter **32**, 415303 (2020).
[31] H. Tan, Y. Xu, J. Wang, J.-F. Liu, and Z. Ma, Journal of Physics D: Applied Physics **54**, 105303 (2020).
[32] A. Iurov, L. Zhemchuzhna, G. Gumbs, D. Huang, P. Fekete, F. Anwar, D. Dahal, and N. Weekes, Scientific reports **11**, 1 (2021).
[33] L. Hao, Physical Review Materials **6**, 034002 (2022).
[34] Y.-R. Chen, Y. Xu, J. Wang, J.-F. Liu, and Z. Ma, Physical Review B **99**, 045420 (2019).
[35] V. Gusynin, S. Sharapov, and J. Carbotte, Journal of Physics: Condensed Matter **19**, 026222 (2006).
[36] G. Gumbs, A. Iurov, D. Huang, and L. Zhemchuzhna, Physical Review B **89**, 241407 (2014).
[37] M. Amado, E. Diez, F. Rossella, V. Bellani, D. López-Romero, and D. K. Maude, Journal of Physics: Condensed Matter **24**, 305302 (2012).
[38] A. Iurov, D. Huang, G. Gumbs, W. Pan, and A. Maradudin, Physical Review B **96**, 081408 (2017).
[39] H. Xue, Y. Yang, F. Gao, Y. Chong, and B. Zhang, Nature materials **18**, 108 (2019).
[40] S. Mukherjee, A. Spracklen, D. Choudhury, N. Goldman, P. Öhberg, E. Andersson, and R. R. Thomson, Physical review letters **114**, 245504 (2015).
[41] Z. Li, J. Zhuang, L. Wang, H. Feng, Q. Gao, X. Xu, W. Hao, X. Wang, C. Zhang, K. Wu, et al., Science advances **4**, eaau4511 (2018).
[42] N. Goldman, D. Urban, and D. Bercioux, Physical Review A **83**, 063601 (2011).
[43] A. Julku, S. Peotta, T. I. Vanhala, D.-H. Kim, and P. Törmä, Physical review letters **117**, 045303 (2016).
[44] T. J. Constant, S. M. Hornett, D. E. Chang, and E. Hendry, Nature Physics **12**, 124 (2016).
[45] X. Yao, M. Tokman, and A. Belyanin, Physical review letters **112**, 055501 (2014).
[46] M. Orlita, D. Basko, M. Zholudev, F. Teppe, W. Knap, V. Gavrilenko, N. Mikhailov, S. Dvoretskii, P. Neugebauer, C. Faugeras, et al., Nature Physics **10**, 233 (2014).
[47] C. Abilio, P. Butaud, T. Fournier, B. Pannetier, J. Vidal, S. Tedesco, and B. Dalzotto, Physical Review Letters **83**, 5102 (1999).
[48] N. A. Franchina Vergel, L. C. Post, D. Sciacca, M. Berthe, F. Vaurette, Y. Lambert, D. Yarekha, D. Troadec, C. Coinon, G. Fleury, et al., Nano Letters **21**, 680 (2020).
[49] B. R. Ortiz, P. M. Sarte, E. M. Kenney, M. J. Graf, S. M. Teicher, R. Seshadri, and S. D. Wilson, Physical Review Materials **5**, 034801 (2021).
[50] S.-L. Yu and J.-X. Li, Physical Review B **85**, 144402 (2012).
[51] T. Neupert, M. M. Denner, J.-X. Yin, R. Thomale, and M. Z. Hasan, Nature Physics **18**, 137 (2022).
[52] Y. Cao, V. Fatemi, S. Fang, K. Watanabe, T. Taniguchi, E. Kaxiras, and P. Jarillo-Herrero, Nature **556**, 43 (2018).
[53] M. Yankowitz, S. Chen, H. Polshyn, Y. Zhang, K. Watanabe, T. Taniguchi, D. Graf, A. F. Young, and C. R. Dean, Science **363**, 1059 (2019).
[54] H. B. Heersche, P. Jarillo-Herrero, J. B. Oostinga, L. M. Vandersypen, and A. F. Morpurgo, Solid State Communications **143**, 72 (2007).
[55] S. Cunha, D. da Costa, J. M. Pereira Jr, R. Costa Filho, B. Van Duppen, and F. Peeters, Physical Review B **104**, 115409 (2021).
[56] O. Kibis, Physical Review B **81**, 165433 (2010).
[57] K. Kristinsson, O. V. Kibis, S. Morina, and I. A. Shelykh, Scientific reports **6**, 1 (2016).
[58] A. Iurov, L. Zhemchuzhna, G. Gumbs, D. Huang, W.-K. Tse, K. Blaise, and C. Ejiogu, Scientific Reports **12**, 1 (2022).
[59] K. F. Mak, K. L. McGill, J. Park, and P. L. McEuen, Science **344**, 1489 (2014).
[60] Z. Ye, D. Sun, and T. F. Heinz, Nature physics **13**, 26 (2017).
[61] G. Wang, X. Marie, B. Liu, T. Amand, C. Robert, F. Cadiz, P. Renucci, and B. Urbaszek, Physical review letters **117**, 187401 (2016).
[62] E. Hwang and S. D. Sarma, Physical Review B **79**, 165404 (2009).
[63] A. Iurov, L. Zhemchuzhna, D. Dahal, G. Gumbs, and D. Huang, Physical Review B **101**, 035129 (2020).
[64] K. Ziegler, Physical Review B **75**, 233407 (2007).
[65] T. Stauber, N. Peres, and A. Geim, Physical Review B **78**, 085432 (2008).
[66] F. Pellegrino, G. Angilella, and R. Pucci, Physical Review B **81**, 035411 (2010).
[67] L. Stille, C. J. Tabert, and E. J. Nicol, Physical Review B **86**, 195405 (2012).
[68] A. Iurov, G. Gumbs, and D. Huang, Physical Review B **98**, 075414 (2018).
[69] D. Oriekhov and V. Gusynin, Physical Review B **106**, 115143 (2022).
[70] S. A. Herrera and G. G. Naumis, Physical Review B **101**, 205413 (2020).
[71] C.-Y. Tan, C.-X. Yan, Y.-H. Zhao, H. Guo, H.-R. Chang, et al., Physical Review B **103**, 125425 (2021).
[72] M. Gibertini, F. M. Pellegrino, N. Marzari, and M. Polini, Physical Review B **90**, 245411 (2014).
[73] Z. Li and J. P. Carbotte, Phys. Rev. B **86**, 205425 (2012).
[74] A. Carvalho, R. M. Ribeiro, and A. H. Castro Neto, Phys. Rev. B **88**, 115205 (2013).

[75] S. Verma, A. Mawrie, and T. K. Ghosh, Physical Review B **96**, 155418 (2017).
[76] B. Napitu, Journal of Applied Physics **127**, 034303 (2020).
[77] C. J. Tabert and E. J. Nicol, Physical Review B **87**, 121402 (2013).
[78] C. J. Tabert and E. J. Nicol, Physical Review Letters **110**, 197402 (2013).
[79] C. J. Tabert and E. J. Nicol, Physical Review B **88**, 085434 (2013).
[80] T. Biswas and T. K. Ghosh, Journal of Physics: Condensed Matter **28**, 495302 (2016).
[81] Z. Li, E. A. Henriksen, Z. Jiang, Z. Hao, M. C. Martin, P. Kim, H. L. Stormer, and D. N. Basov, Nature physics **4**, 532 (2008).
[82] K. F. Mak, M. Y. Sfeir, Y. Wu, C. H. Lui, J. A. Misewich, and T. F. Heinz, Physical review letters **101**, 196405 (2008).
[83] J. P. Carbotte, E. Schachinger, and J. Hwang, Physical Review B **71**, 054506 (2005).
[84] P. de Vries, K. Michielsen, and H. De Raedt, Zeitschrift für Physik B Condensed Matter **95**, 475 (1994).
[85] E. Mishchenko, Physical review letters **98**, 216801 (2007).
[86] M. Vigh, L. Oroszlány, S. Vajna, P. San-Jose, G. Dávid, J. Cserti, and B. Dóra, Physical Review B **88**, 161413 (2013).
[87] B. Dey and T. K. Ghosh, Physical Review B **99**, 205429 (2019).
[88] N. Weekes, A. Iurov, L. Zhemchuzhna, G. Gumbs, and D. Huang, Physical Review B **103**, 165429 (2021).
[89] N. J. Horing, M. Glasser, and J. D. Mancini, Physica Scripta **96**, 015806 (2020).
[90] C. Grazianetti, S. De Rosa, C. Martella, P. Targa, D. Codegoni, P. Gori, O. Pulci, A. Molle, and S. Lupi, Nano letters **18**, 7124 (2018).